EFFICIENT WAVELENGTH TUNING TECHNIQUES FOR INTEGRATED SILICON PHOTONICS

A Thesis

by

ALEX KWASI NYAVOR TITRIKU

Submitted to the Office of Graduate and Professional Studies of
Texas A&M University
in partial fulfillment of the requirements for the degree of

MASTER OF SCIENCE

Chair of Committee,	Samuel Palermo
Committee Members,	Edgar Sanchez-Sinencio
	Krishna Narayanan
	Yoonsuck Choe
Head of Department,	Chanan Singh

December 2014

Major Subject: Electrical Engineering

ABSTRACT

The past decade has seen a significant amount of academic and industrial research into interconnect topologies that employ optical channels for next generation high speed communication systems. Integrated optical interconnects have taken center stage in tackling channel loss limitations of traditional electrical links and bandwidth requirements for inter-chip and intra-chip signal processing for multi-core processors. Wavelength-division multiplexing (WDM) optical interconnect architectures based on microring resonator devices offer a low-area and energy-efficient approach to realize both high-speed modulation and WDM with high-speed transmit-side ring modulators and high-Q receive-side drop filters.

At the heart of silicon photonics is the silicon microring resonator. These high-Q refractive devices can achieve high contrast ratios with their small footprint and enable distance independent communication. A major challenge to the use of microring resonators is the sensitivity of their resonance wavelength to process and fabrication imperfections and temperature perturbations. To curtail the effects of resonance wavelength drifts, stabilization schemes are implemented to properly align the resonance wavelength of the microring device with the input laser wavelength.

This thesis work focuses on three main issues. Firstly, the sources and effects of mismatch in silicon microring resonators are identified. Secondly, a review of literature is done to examine existing resonance wavelength stabilization techniques. Based on the reference search tuning algorithm, a new dual-loop tuning method which combines the benefits of bias-based and thermal-based tuning schemes is proposed. Furthermore, we evaluate the tuning efficiency of some existing and the proposed tuning schemes using a statistical model to determine optimal power and

speed efficiency. Modeling results of carrier injection ring resonator devices with common thermal tuning and the new dual-bias/thermal scheme reveals that the latter scheme offers $\sim 50\%$ improvement in power with small variations and close to 16X speed improvement.

Finally, the tuning control loop is fabricated in GP 65nm CMOS process. Transmit-side and receive-side are independently implemented for a 5-channel WDM system. Measurement results are presented in both cases. The transmitter IC achieved both static and dynamic tuning, stabilizing ring resonance wavelength in the midst of temperature fluctuations from an adjacent ring. The total power consumed was 5.17mW while covering a wavelength tuning range of $\sim 0.8nm$. Static tuning was succesfully demonstrated for the receiver IC. A tuning range of $0.7nm$ was achieved over a $2mA$ dynamic range of current.

DEDICATION

To my sovereign King and Savior Jesus Christ

and to the memory of my late parents, Benedicta and Philip

ACKNOWLEDGEMENTS

My time and study as a student in Texas A&M University has been a pleasant one thanks to the generosity of many wonderful people. I start by thanking my advisor, Dr. Samuel Palermo for agreeing to be my advisor and giving me the opportunity to contribute to this exciting field of silicon photonics. In addition to his excellent mentorship and insight, he continuously challenges me to give my best output. I also sincerely thank Dr. Edgar Sanchez-Sinencio, Dr. Krishna Narayanan and Dr. Choe Yoonsuck for serving as members on my thesis committee. Your time and valuable feedback are most appreciated.

Fellow colleague graduate students I worked with in my research group were instrumental in making this work a success. I am particularly grateful to Ayman Shaffik, Cheng Li, and Ehsan Zhian Tabasy. Not to forget the support and encouragement of other students in the Analog and Mixed Signal Center. I cannot fail to mention the friendship and encouragement of my roommates Roland Ribeiro and Gideon Adom-Bamfi. You made the past two years an enjoyable and memorable journey.

My graduate studies in Texas A&M was made possible and funded by Texas Instruments (TI). My thanks particularly goes to Tuli Dake, Ben Sarpong, Dee Hunter and Art George all of TI who played an active role in initiating the African Analog University Relations Program (AAURP) which is in fact the channel for sponsoring my masters education.

Finally, I would like to thank my family and friends for their unconditional and ever assuring support and encouragement. I am particularly thankful to my siblings for the many sacrifices they have made for me. My love is always with you.

NOMENCLATURE

Acronyms

ADC	Analog-to-Digital Converter
ARM	Adiabatic Resonant Microring
BER	Bit Error Rate
BHD	Balanced Homodyne Detection
CMOS	Complimentary Metal Oxide Semiconductor
DAC	Digital-to-Analog Converter
ER	Extinction Ratio
FSM	Finite State Machine
I/O	Input and Output
IC	Integrated Circuit
LSB	Least Significant Bit
MR	Microring Resonator
MSB	Most Significant Bit
MSM	Metal Semiconductor
MZI	Mach-Zehnder Interferometer
FPGA	Field Programmable Gate Array
FSR	Free Spectral Range
FWHM	Full Width Half Maximum
PD	Photodiode
PWM	Pulse Width Modulation
Q	Quality Factor
QCSE	Quantum-Confined Stark effect

RX	Receiver
SDM	Sigma-Delta Modulation
SOI	Silicon-on-Insulator
TIA	Transimpedance Amplifier
TX	Transmitter
WDM	Wavelength Division Multiplexing

TABLE OF CONTENTS

Page

LIST OF FIGURES

FIGURE Page

LIST OF TABLES

1. INTRODUCTION

The growing speed and power requirements for data processing and computation has pushed for higher bandwidth demands for both intra- and inter-chip communication. Inter-chip input-output (I/O) bandwidth however has not kept up with processing performance scaling [13]. Although transceiver circuits can operate in the Gb/s range, channel characteristics have been a major limitation to link performance.

The frequency dependent loss of electrical interconnects coupled with signal crosstalk and loss due to impedance mismatch have posed a major challenge in their use for high-speed I/O link designs. Multiple high-speed links and complex equalization techniques need to be employed to compensate for the loss of band-limited electrical channels in order to achieve good data integrity and high BERs required in many high-speed applications [14].

Optical interconnects are emerging as a potential substitute to traditional electrical interconnects in building next-generation communication systems, attracting substantial research in recent years. With their ability to provide much greater bandwidth, lower power consumption, decreased interconnect delays, resistance to electromagnetic interference and reduced signal crosstalk [15], optical interconnects are suitable for dense and more energy-efficient interconnect systems. Silicon photonics allows for the use of a single waveguide to host multiple data channels by wavelength-division multiplexing (WDM) [16]. A key component in silicon photonic links is the microring resonator (MR). Ring resonator based photonic links make possible distance-independent connectivity whose bandwidth scales with the degree of WDM.

The resonant wavelength of these high-Q silicon MRs however is very susceptible

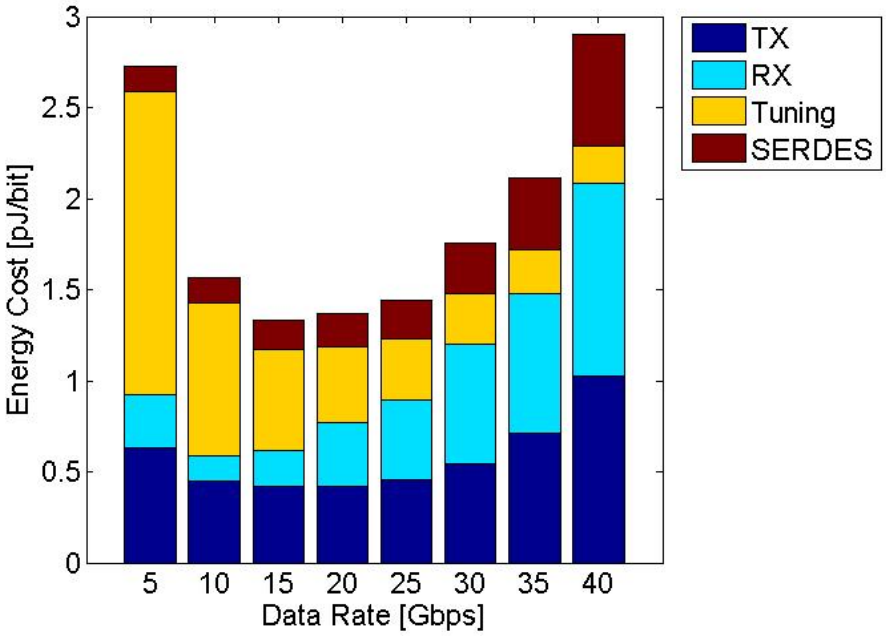

Figure 1.1: Energy cost assuming 65nm CMOS and $1\sigma = 1nm$

to fabrication errors and temperature variations [17,18]. Resonance wavelength drift affects the performance of the MR. This prompts the need for dynamic resonant wavelength tuning which can be achieved by adjusting the refractiive index of the ring resonator device thermally, electrically or both. Tuning however comes at an energy cost and speed penalty. As can be seen in Fig. 1.1, at lower data rates, a large portion of the overall link power budget is dominated by tuning power and with devices displaying time constants in the range of $100\mu s$, tuning speed could become critical in high I/O count systems. This has motivated extensive research into device and system design to improve both power efficiency and tuning speed of tuning techniques for practical low power silicon photonic links.

This thesis examines the causes and effects of resonance wavelength drifts in silicon MRs and does a comparative analysis of existing wavelength stabilization

schemes. New tuning techniques that make for power efficient and fast tuning are proposed. Key algorithms and circuit blocks needed for tuning are discussed as well.

1.1 Organization

In order to understand the source of mismatch in resonance wavelength of silicon ring devices, a proper background in the nature and composition of silicon MRs is necessary. Section 2 therefore presents an overview of optical links. Different blocks within the silicon photonic platform are described. The nature of variations and their effect on the resonance frequency of silicon MRs are also discussed. Also covered in this section are some state-of-the art work in tuning for silicon MRs.

Section 3 delves into tuning efficiency modelling and comparison of existing tuning mechanisms. Different tuning schemes are examined based on their merits and demerits. The tuning model methodology is presented and key results are discussed.

Section 4 focuses on tuning systems. Tuning circuitry design and simulations are presented. Also discussed are the considerations to be taken into account in implementing both transmitter and receiver side tuning. Proposed tuning schemes are verified and experimental results are presented as well.

Finally, in Section 5 a summary of the conclusion of this work is presented.

2. BACKGROUND

Before delving into the intricacies of silicon MRs, it is important to understand the various blocks and components that come together to form a high speed optical WDM link. This section provides an overview of the silicon photonic devices. We investigate the basic structure and principle of the ring resonator and identify the types that exist. Sources and effects of non-idealities in silicon MRs are also discussed. We also take a look at a silicon ring resonator based WDM link. The section ends with a discussion of some existing resonance wavelength tuning algorithms and the proposed reference search tuning algorithm.

2.1 Silicon Photonic Components

2.1.1 Optical Modulators

Modulation involves altering the fundamental dynamics of a substance. In much the same way as electrical modulation exists in electrical links, optical modulation is pivotal in optical links. Optical modulation in simple terms is the modulation of a light source internally (directly) or by external means. Although direct modulation can be compact, straightforward and inexpensive, external modulation is more advantageous. External modulation allows for higher speed operation, low chirp effect, large extinction ratio and the flexibility to allow for both amplitude and phase modulations [15, 19].

Optical modulators are devices that can alter different parameters such as amplitude, phase or the polarity of a light beam. This modification of light can be the result of exposing the modulator to some physical effect such as an electric field, temperature change or an acoustic wave. A number of mechanisms exist to electrically manipulate the refractive index of modulating materials, the common ones being

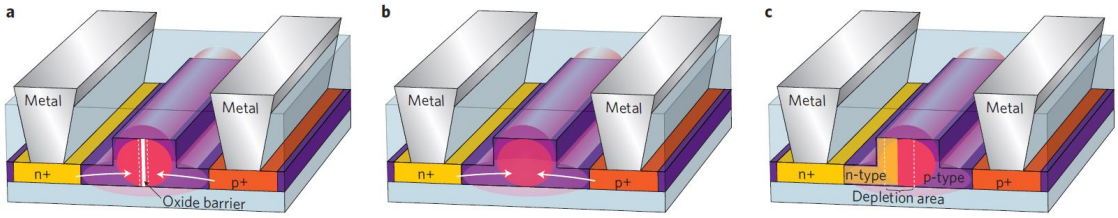

Figure 2.1: Cross-sections of silicon optical modulator device structures - (a) carrier accumulation (b) carrier injection and (c) carrier depletion mode devices [1]

the Franz-Keldysh effect, the quantum-confined Stark effect (QCSE) and the Kerr effect [19]. These however have been shown to be weak in pure silicon and hence require the introduction of a secondary material which complicates the design process. The plasma dispersion effect which achieves a change in both the real and imaginary parts of the refractive index by the concentration of free charges has been identified as the most common effect used in modulating silicon optical modulators [1].

Depending on how charge carriers are manipulated using the plasma dispersion effect, three types of modulators can be realized. These are the carrier accumulation, carrier injection and carrier depletion devices.

As seen in Fig. 2.1(a), carrier accumulation based devices are in simple terms equivalent to a MOS capacitor where the two doped halves of the waveguide structure are separated with a thin insulating layer of SiO_2. Light absorption by accumulation of carriers is not sufficiently strong in the telecommunication wavelengths of $1.3\mu m$ and $1.55\mu m$ [20] hence carrier accumulation based devices are the least common among the three.

Carrier injection mode devices are $p-i-n$ junction based devices. The heavily doped p-type and n-type regions are separated by an intrinsic area which defines the waveguide region as shown in Fig. 2.1(b). The device operates in forward bias

mode where free charge carriers are injected into the intrinsic region resulting in a change in the refractive index. Carrier injection devices allow for low insertion loss operation, high extinction ratios and are highly tunable. However they exhibit a low bandwidth which is limited by the long lifetime of minority charge carriers.

Carrier depletion devices (Fig. 2.1(c)) on the other hand operate as a PN junction in reverse biase mode. By applying a reverse bias voltage, the depletion region in the waveguide becomes larger [19]. Depletion mode devices are suitable for higher modulation speeds compared to carrier injection devices due to their reliance on electric-field induced majority carrier dynamics but device speed is majorly limited by the RC constant [21]. However due to its limited modulation depth it has a higher insertion loss and very limited tunability.

Three important parameters that characterize the performance of optical modulators are defined below;

Extinction Ratio (ER) - also referred to as the modulation depth, is defined as the ratio of the output power of the device when it is in ON state to when it is in OFF state [15]. It is mostly expressed in decibels (dB) and sometimes as percentage. A high ER is required to achieve good receiver sensitivity and BER.

Bandwidth - the modulation bandwidth or speed is the defined as the frequency at which the modulation is reduced to 50% of its maximum value [19]. High data rate links require very high modulation speeds.

Insertion Loss - this metric encapsulates the total loss of the device when used in a photonic circuit. It includes loss due to reflection, absorption, coupling and is significant because of its effect on the overall link budget [19]. Typical values are in the range of $5 - 7dB$.

There is an inherent trade-off between these parameters. The insertion loss increases with device length whereas the bandwidth is inversely related to the device

length. The insertion loss also trades-off with the ER [15]. Other important features that are considered in the choice of optical modulators are the power consumption and the footprint of the device.

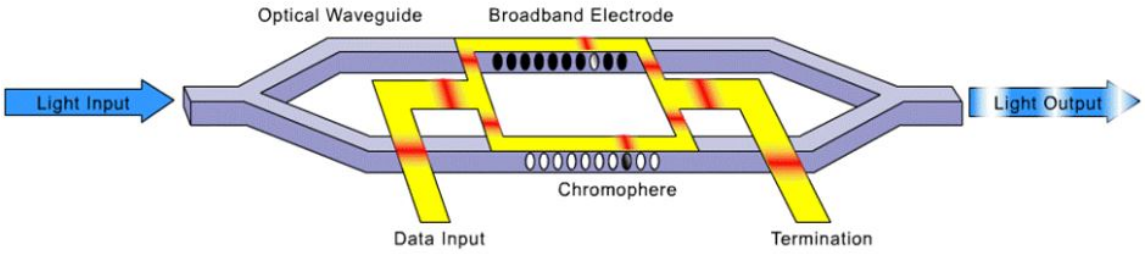

Figure 2.2: A Mach-Zehnder Interferometer [2]

There are two main optical modulators that convert an alteration in refractive index to intensity modulation based on the plasma dispersion effect. Firstly is the Mach-Zehnder interferometers (MZI) shown in Fig. 2.2 which is mainly useful for phase modulation. Even though they are wavelength insensitive, they occupy large footprints ($\sim 10^4 \mu m^2$) and have poor power efficiency. The second type is the ring resonator based modulators which modify the refractive index based on the resonant condition [19]. They offer the advantage of relatively small size and hence are suitable for densed WDM applications and have a higher power efficiency. In the next section, ring resonator based optical modulators are discussed into more detail

2.1.2 Silicon Microring Resonator

An optical ring resonator is a looped structure constructed from an optical waveguide that is bent over itself. These high-Q devices are refractive in nature and can

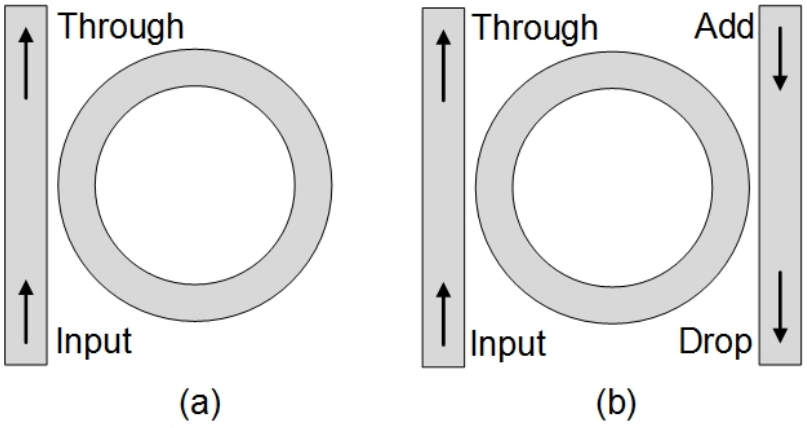

Figure 2.3: Microring resonator configured as (a) a Notch filter (b) an add-drop filter

achieve very high contrast ratios with small dimensions. In order to modulate a transmitted signal using the ring resonator, the refractive index of the highly confined ring structure is modified by electrical signaling which induces a sharp tuning in the resonance wavelength that leads to strong modulation depth changes at or near resonance [22]. Resonance occurs when the whole number of wavelengths is equal to the optical path length. In order to be used in an application, the ring has to be coupled to a straight bus waveguide. Depending upon the number of straight waveguides it is coupled to, the MR can be configured as a notch (all-pass) filter or an add-drop filter. Fig. 2.3 illustrates a microring resonator in both configurations.

When a light source is applied to the input port of the waveguide, part of it travels through to the through port and part of the light is coupled into the optical ring resonator. The transmission power P_{t1} at the output of waveguide of the ring in a notch filter configuration is obtained as [23]

$$P_{t1} = \frac{\alpha^2 + |t|^2 - 2\alpha|t|\cos(\theta + \psi_t)}{1 + \alpha^2|t|^2 - 2\alpha|t|\cos(\theta + \psi_t)} \tag{2.1}$$

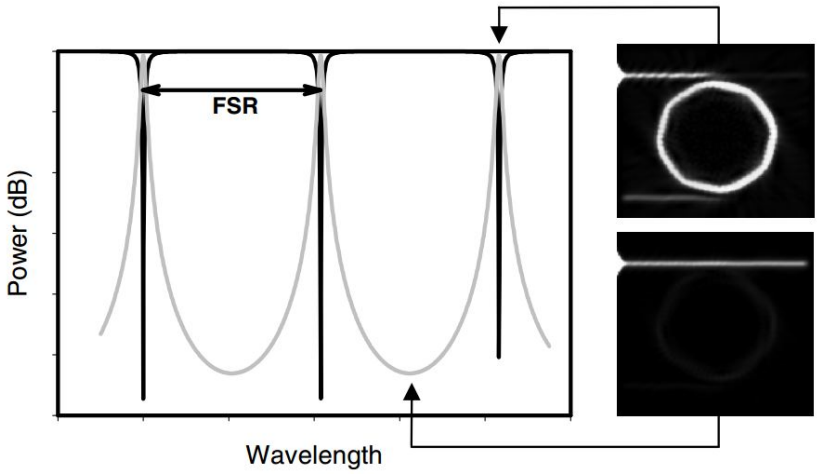

Figure 2.4: Transmission spectra of a double coupled waveguide MR [3]

where α is the loss coefficient of the ring, $|t|$ represents the coupling losses and ψ_t the phase of the coupler. At resonance, $(\theta + \psi_t) = 2\pi m$, where m is an integer, the transmission power becomes [23]

$$P_{t1} = \frac{(\alpha - |t|)^2}{(1 - \alpha|t|)^2} \tag{2.2}$$

In the add-drop configuration, the output power at the drop port of the ring at resonance is given by [23]

$$P_{t2} = \frac{(1 - |t_1|^2) \cdot (1 - |t_2|^2) \cdot \alpha}{(1 - \alpha|t_1 t_2|)^2} \tag{2.3}$$

Microring resonators are able to support multiple resonances which are spaced at wavelength intervals referred to as the free spectral range (FSR) as shown in Fig. 2.4.

The FSR which is a function of the resonant wavelength and the radius of the ring is defined as:

$$FSR = \frac{\lambda^2}{n_g L} \tag{2.4}$$

where L is the circumference of the ring or a round trip length and the n_g is the group refractive index which accounts for the wavelength dependent nature of the effective refractive index of the ring as shown in equation 2.5

$$n_g = n_{eff} - \lambda_0 \frac{dn_{eff}}{d\lambda} \tag{2.5}$$

An important parameter that characterizes the resonance spectrum of the ring resonator is the resonance width. The full width at half maximum (FWHM) also known as the 3 dB bandwidth $2\delta\lambda$ of the resonance lineshape [23] is defined by

$$FWHM = 2\delta\lambda = \frac{\kappa^2 \lambda^2}{\pi L n_{neff}} \tag{2.6}$$

where κ is the normalized coupling coefficient of the coupler between the straight and circular waveguides.

The next parameter of importance is the finesse which is defined as the ratio of the FSR and the resonance width

$$F = \frac{FSR}{FWHM} \tag{2.7}$$

Closely related to the finesse is the quality factor Q of the ring resonator. It is a measure of the sharpness of the resonance with respect to its central frequency [24].

$$Q = \frac{\lambda}{FWHM} \tag{2.8}$$

The Q-factor can also be regarded as the stored energy divided by the power lost

per optical cycle [23].

2.1.3 Waveguide Photodetector

A photodetector is a device used for optical-to-electrical conversion. The photodiodes (PD) generate a current which is proportional to photons absorbed from an incident light. Bandwidth of photodetectors is an essential parameter. In order to achieve high data rate operations, the input capacitance of the photodetector must be kept small enough. This presents an inherent trade-off between the bandwidth and the responsivity (the amount of photocurrent produced per watt of input optical power [25]) of the device.

Typically, photodetectors have been made of $p - i - n$ diodes. Due to the area trade-off between having a high bandwidth and achieving good photo response, conventional lateral $p - i - n$ photodiodes however are not suitable for integrated photonics. Recent years have seen the development of alternate device structures that promise high bandwidth and responsitivity such as metal-semiconductor-metal (MSM) diodes [25] and SiGe based photodetectors [26].

2.2 Ring Resonator Based High Speed WDM Links

One fundamental advantage of optical communication is the ability to multiplex several different wavelengths onto a single waveguide and to be able to demultiplex them via WDM. With their small footprint, by cascading a number of MRs along the same waveguide bus, the MR naturally lends itself for WDM operation.

Fig. 2.5 illustrates a silicon based integrated WDM link. A multi-wavelength comb laser is coupled onto the chip using an optical coupler. In the ring modulator bank, the MRs encode the data onto their respective resonant wavelengths. The modulated signals are then propagated along the waveguide until they reach a matching drop ring filter of specific wavelength in the filter bank. The signal is then

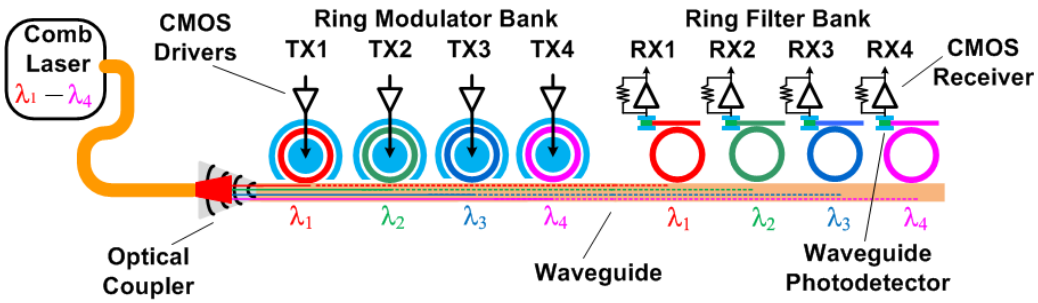

Figure 2.5: Silicon MR based WDM link [4]

converted back to the electrical domain using a PD for the optical receiver to form a bit decision.

2.3 Microring Device Mismatches

Assuming the mth resonant wavelength λ of an MR is given as [5]:

$$n_{eff} \cdot L = m \cdot \lambda \tag{2.9}$$

where n_{eff} is the effective refractive index and L is a round trip length, a simple derivative of equation 2.9 can yield [5]

$$\frac{\delta\lambda}{\lambda} = \frac{\delta L}{L} + \frac{\delta n_{eff}}{n_{eff}} \tag{2.10}$$

From 2.10, it is evident that variations ($\delta\lambda$) in resonant wavelength can arise either from the effective index δn_{eff} variation or variations in the device perimeter length δL [5].

As mentioned earlier, the effective index n_{eff} is very sensitive to device and fabrication error and has a high thermal susceptibility. Non-idealities resulting from device and process tolerance are classified as static and can be relatively large (up to

$\pm 10nm$) whereas those due to temperature fluctuations are classified as dynamic and are relatively small (under $\pm 1nm$ with $\pm 10°$C) [5,17]. Ring resonant wavelength shift standard deviations in WDM links can be local where each ring's wavelength drift is uncorrelated with the adjacent ring. There also exists the possibility of systematic standard deviations where there is global shift in resonant wavelength across all rings in a particular direction [16].

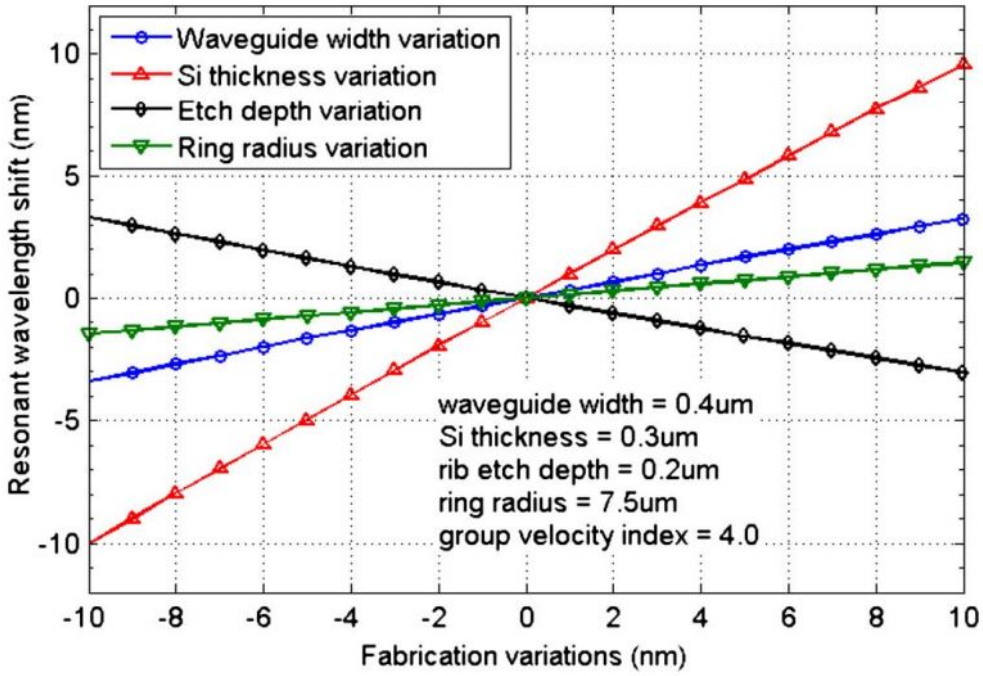

Figure 2.6: Resonant wavelength shift due to manufacturing imperfections [5]

The main factors that contribute to manufacturing variations include variations in waveguide width, silicon layer thickness, etch depth, material stress and interface roughness. [5] reports resonant wavelength shifts of upto $\pm 14nm$ due to variations in silicon thickness. As can be seen in Fig. 2.6, waveguide width and etch depth

variations can result in upto $\pm 5nm$ drift in resonant wavelength.

Ring variations due to fabrication and manufacturing errors also depend largely on the type of wafer employed. Gate poly-silicon on CMOS bulk process has been observed to have same die mismatches of up to 100GHz and absolute frequency variation across wafer of 600GHz [27]. Moreover, restricting fabrication to a smaller area of one wafer, though not economical when it comes to yield and cost, can be one way to improve resonant wavelength disparities.

The other two manufacturing parameters that affect the effective index of the resonant optical device are very related to optical lithography tools and processes employed in device fabrication [28]. Using a finer CMOS fabrication tool, [29] achieved a smaller wavelength shift $7.5nm$ of 3σ variation in waveguide width. Many successful studies have also been made into creating cascaded microrings with varying resonant wavelengths in different substrates such glass [30], SiN [31] and silicon-on-insulator (SOI) substrates [32–34]. A good way to control manufacturing variations will be to employ static tuning. More on this will be discussed in the subsequent section.

Dynamic mismatches arise due to the strong dependence of the refraction index of silicon ring resonators on temperature. The high thermo-optic coefficient of silicon ($1.86 \times 10^{-4} K^{-1}$) coupled with the wavelength selectivity of MRs make them even more vulnerable to temperature fluctuations [18]. The change in resonant wavelength of a silicon MR with respect to temperature can be simply given as:

$$\frac{d\lambda}{dT} = \frac{\delta n_{eff}}{\delta T} \frac{\lambda_o}{n_g} \tag{2.11}$$

where n_{eff} is the effective index, n_g the group index and λ_o the resonant wavelength. The resonant wavelength is thus sensitive not only to changes in the absolute temperature but more importantly to the relative changes in temperature when the

microring is in operation in an optical link [35]. It is vital to note that due to the high sensitivity of resonant wavelength to temperature, MR based devices may not work within typical microelectronic temperature ranges. Temperature changes > 1K are sufficient to render the ring device inoperable [36,37]. [27] has reported frequency drifts due to thermal variations in the range of -10GHz/K. Due to the time dependent nature of the dynamic offsets, active (dynamic) tuning needs to be implemented to compensate for ring non-idealities.

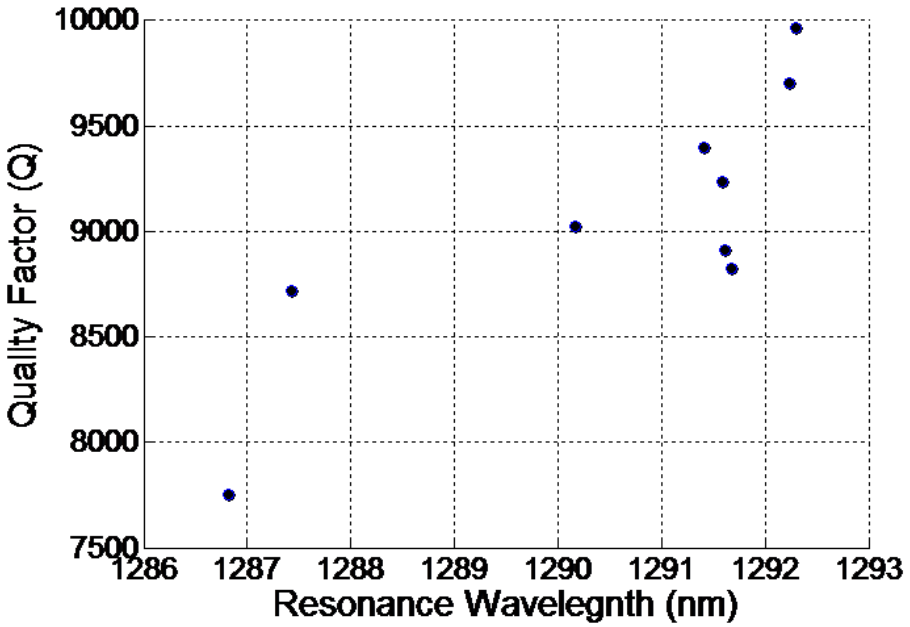

Figure 2.7: Measured Q-factor vs resonance wavelength of nine MRs [4]

A major consequence of resonant wavelength shift on MRs is the degradation in the Q -factor of the device. As seen in Fig. 2.7, for a $2.5\mu m$ radius MRs fabricated on a 130 nm CMOS SOI wafer, the Q-factor varies from 7750 to 10000 across a

5.48nm wavelength spread. Another repercussion of resonant wavelength shift is poor extinction ratio.

2.4 Resonance Wavelength Tuning

As discussed earlier, microring non-idealities require tuning of resonant wavelengths to achieve better performance. It is essential to device a means to measure and monitor the drift in the resonant wavelength of the MR, and a feedback system to adjust and control the resonant wavelength by whichever method that is used. This has given rise to many control-based solutions and algorithms for stabilizing the resonant wavelength. These control-based schemes generally have a sensing mechanism and a closed loop feedback control to adjust ring wavelength. An ideal system should be highly compatible with WDM and must simple and easy to implement. It must be able to operate in the midst of multiple data carriers in a WDM network. Each of these schemes can be analyzed on the power needed, the speed of stabilization and the ease of implementation. Some of these solutions in addition to our proposed and verified system are discussed below.

2.4.1 Infrared Camera

In [6], C. Qui *et. al* utilizes a digital infrared camera to measure the scattered power from two rings. Using a Labview-based program, the scattered power from the camera is used to control the voltage applied to the micro-heaters for the feedback control. The virtual feedback control system continuously measures the difference in scattering from the two rings and accordingly adjusts the heating current based on the sign of the difference. Fig. 2.8 shows an overview of the system.

Aside the time it will take to achieve resonant wavelength locking, this system is not integrated and thus will be very expensive in terms of both area and cost to scale in a compact manner. The system is also susceptible to fabry-perot interference.

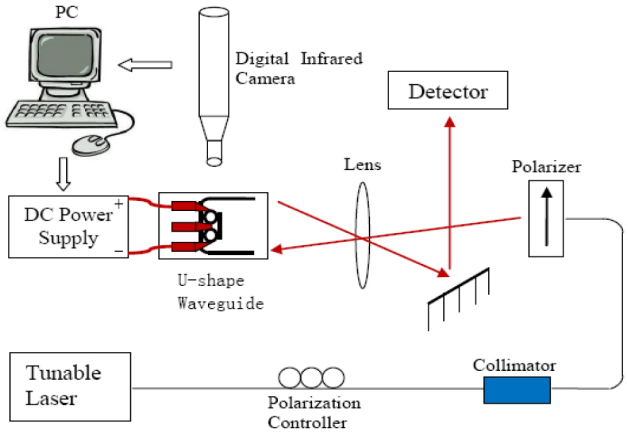

Figure 2.8: Setup for measuring optical scattering for feedback control process [6]

2.4.2 FPGA

E. Timurdogan *et. al* report the first high-speed and scalable on-chip optical wavelength stabilization scheme in [7]. An adiabatic resonant microring (ARM) modulator was used. The setup which is shown in Fig. 2.9 includes a transimpedance amplifier (TIA) which detects the through port intensity, followed by a 100 KHz low pass filter and a 10−bit analog-to-digital converter (ADC) used to digitize the output of the filter. An FPGA then makes a decision based on the digitized word. Based on this decision, a pulse-density-modulated (PDM) signal is generated to tune the power of the integrated heater.

The decision-making control algorithm for wavelength recovery is designed for continuous search of the minimum (for the thru port) or maximum (for the drop port) level. The automated feedback algorithm works with no information about the on/off resonance levels, quality factor and the frequency offset.

This method also does not offer a completely integrated solution. Moreover, the technique reported high wavelength recovery time ($\sim 200\mu s$) and may be vulnerable to fabry-perot interference in the optical path.

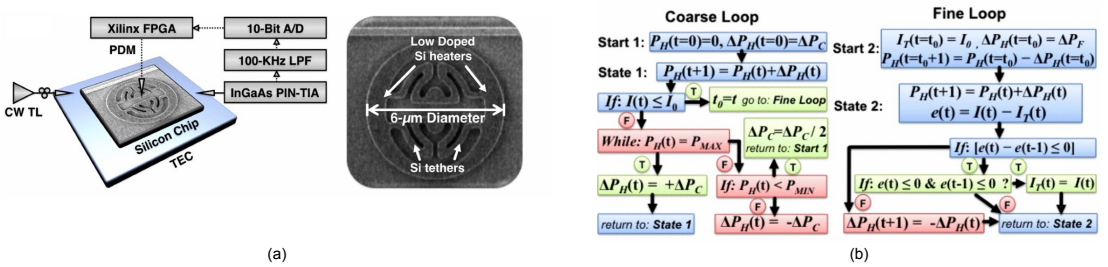

Figure 2.9: (a) Setup for wavelength recovery using an ARM resonator (b) flow charts for wavelength recovery decision making [7]

2.4.3 BER Measurement

Another tuning method that has been demonstrated is using BER measurement by [8]. Independent logic 1 and logic 0 bit errors from a receiver are used to form a decision and a logic circuitry is used to drive an integrated heater. The system block diagram is shown in Fig. 2.10

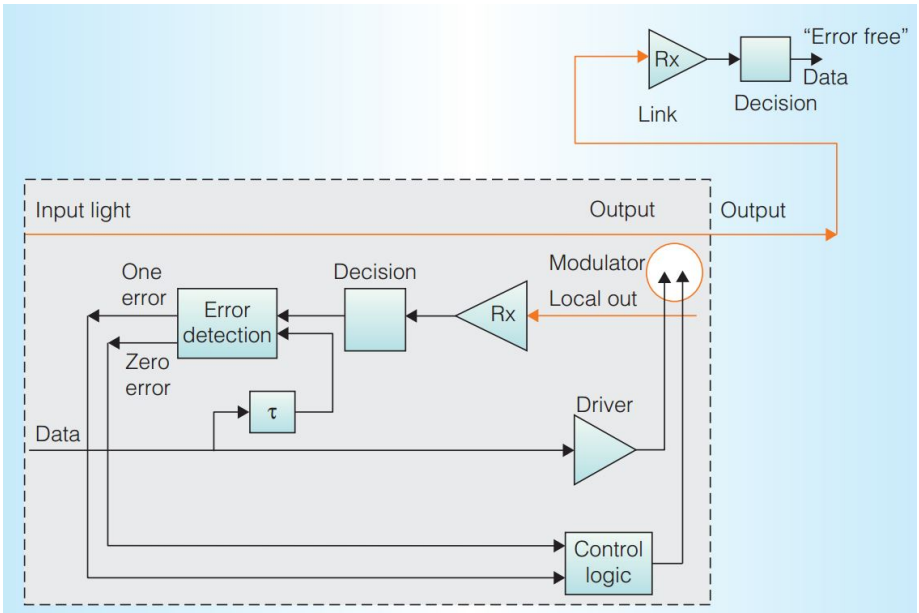

Figure 2.10: Block diagram of BER technique [8]

An XOR gate is used to compare bits detected by a local receiver against what was transmitted by the driver to the modulator. The errors are accumulated to determine which side of the resonance the carrier wave resides. The downside is, BER monitoring is more complicated (requiring circuitry operating at the speed equivalent to the data rate) and this affects overall power-consumption of the system and the ease of implementation.

2.4.4 Homodyne Detection

Muliple techniques have explored the generation of an anti-symmetrical error signal centered about the resonant wavelength. One of such solutions is the use of homodyne detection as reported in [9]. Balanced homodyne detection locking works by using the MR with an interferometric structure such as an MZI. A fraction light coupled to the input port of the MR is interfered with a fraction coupled out from the drop port of the ring resonator. A diagram of the system and a measured error signal are shown in Fig. 2.11.

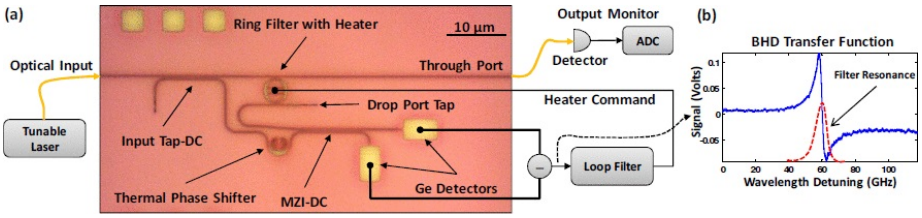

Figure 2.11: (a) Block diagram of homodyne technique (b) measured error signal [9]

The error signal is fed to a loop filter which then controls the tuning heater. The error detection circuitry is implemented off-chip. Even though balanced homodyne detection meets most of the requirements for an ideal tuning control system, the use of an interferometric structure may reduce the ease of implementation as some

configurations of the MR may not be readily compatible [35]. There is also a huge power penalty due to taping part of the input power.

2.4.5 Dithering

K. Padmaraju *et. al* demonstrated the use of the concept of dithering in thermal tuning control [10,38]. The input optical signal is modulated using thermal dithering. The photocurrent generated is converted to voltage by a TIA and then amplified. An analog mixer is then used to mix the amplified signal with the driving dithering signal. The product is low-pass filtered and processed as an error signal which is used to generate the appropriate control to the heater. The block diagram is shown in Fig. 2.12

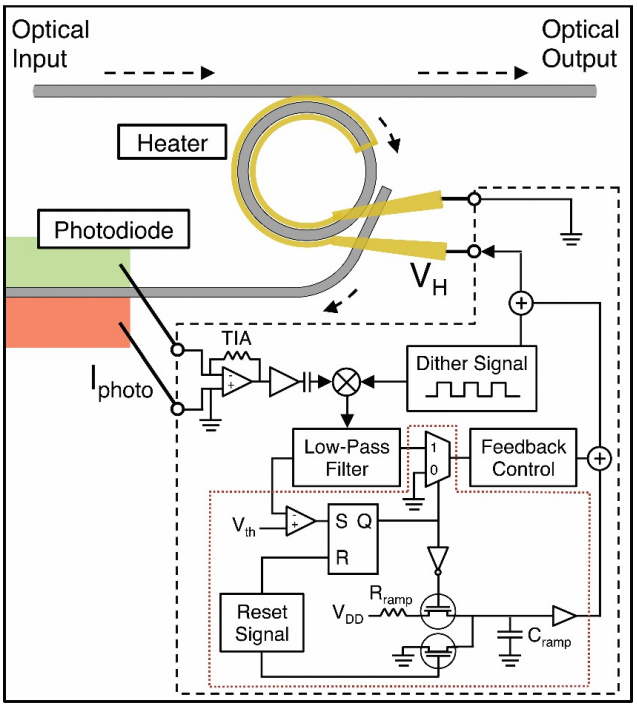

Figure 2.12: Block diagram of dithering technique [10]

Although simple and potentially low power, dithering can reduce the modulation depth of the MR device. Furthermore, the solution is not completely integrated.

2.5 Reference Search Algorithm

The block diagram in Fig. 2.13 and the flow-chart in Fig. 2.14 summarizes the tuning system operation. The tuning process is controlled by an automatic tuning loop. The loop includes both a bias DAC and a thermal DAC. A reference DAC is also available to provide a preset reference with which we compare the output optical power from the ring. The loop is controlled by a digital finite state machine (FSM) whose operation is based on the reference search tuning algorithm. The primary aim of the reference search algorithm is to tune the ring resonator output to a point that maximizes the ER.

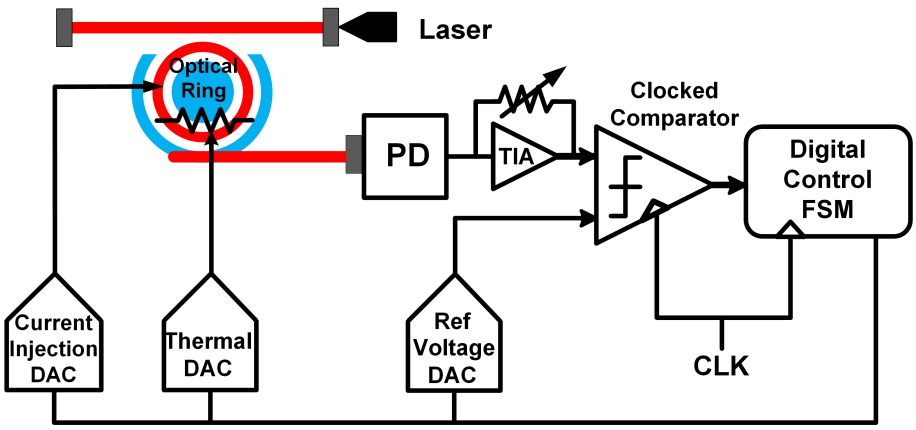

Figure 2.13: Tuning loop

The tuning process starts with defining an initial reference level using the reference DAC. The optical power from the ring is compared with the preset reference level using a comparator. The averaged comparator output is used to determine

whether the ring output power is at the reference point. The tuning DACs are increased till the ring output is locked to initial reference level.

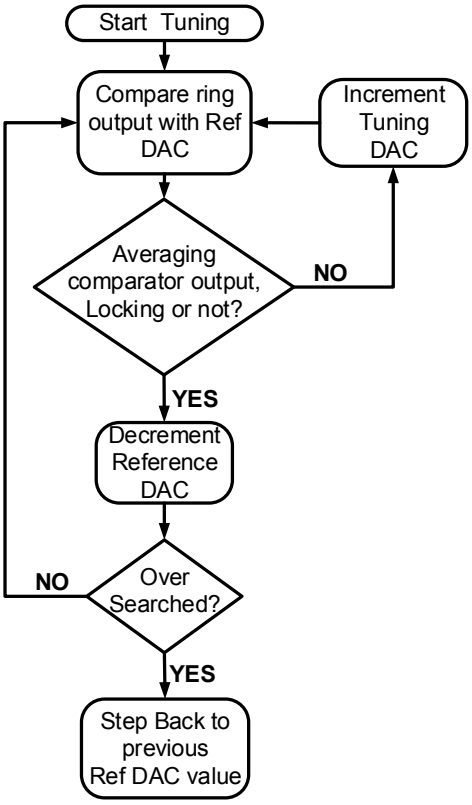

Figure 2.14: Reference search tuning algorithm

The preset reference level might not be the optimal point that will yield the maximum extinction ratio. So the control has a optimal reference search capability. The reference level is stepped down and tuning process continues till maximum extinction ratio is achieved. If the reference level progresses such that it falls outside the ring resonator curve, loss of lock due to over-searching is detected and the reference level is brought back to the previous optimal point.

2.5.1 Dynamic Tuning

The reference search algorithm is capable of both static and dynamic operation. Tuning with randomly modulated data (Fig. 2.15), which obviates bringing the link down, is achieved by utilizing the same procedure. Note that the convergence time increases due to higher digital filtering for sufficient optical power averaging. This tuning mode, however, brings some complications with it. The first issue with dynamic tuning is that the loop will tune to the average power between the logic '0' and logic '1' positions. Also, in order to achieve a similar extinction ratio in dynamic-tuning mode, the modulated resonance shift, between data '0' and data '1' should be larger than the resonators full width half maximum, FWHM.

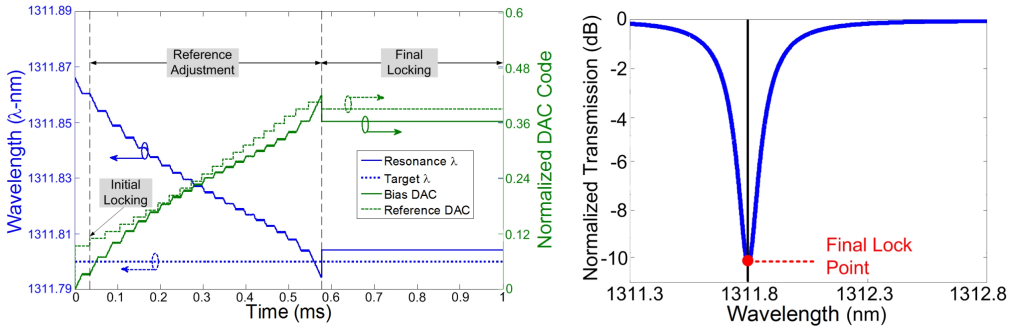

Figure 2.15: Simulation results for dynamic tuning mode [4]

A second complication that comes with dynamic tuning mode is especially important with multi-channel WDM systems, where the number of available lasers may be larger than rings. In this case, a mechanism to distinguish between modulated and unmodulated laser channels is necessary at the receiver, to prevent erroneous tuning to an empty (unused) laser channel and this is given due consideration in the design of the algorithm.

2.6 Summary

Optical interconnects offer great promise to solve low I/O bandwidth challenges posed in electrical interconnects. To make optical interconnect technology compatible with existing silicon processes, devices are needed to power the optical-to-electrical-to-optical signal conversion trail. Some of these devices have been discussed in this section.

Key among them is the silicon microring resonator. Despite its ability to enable densed WDM systems, the sensitivity of the resonance wavelength of this small footprint devices to fabrication imperfections and environmental temperature perturbations causes unpredictable drifts. This puts a constraint on the use of the MR as additional circuits must be employed to curtail the non-ideal effects of such wavelength shifts. Control algorithms for achieving resonance wavelength tuning have been discussed based on their merits and demerits. Table 2.1 shows a comparative summary of the existing tuning mechanisms.

Table 2.1: Tuning mechanisms summary

Mechanism	**Logic/Control**	**Ease of Implementation**	**Power***
Infrared [6]	PC/Software	Difficult to scale	N/R
FPGA [7]	FPGA	High	$< 1mW$
BER [8]	FPGA	Low	$\sim 550\mu W$
Homodyne [9]	Discrete	Low	N/R
Dithering [10]	Discrete	Moderate	$\sim 385\mu W$
Reference search [4]	CMOS	High	$\sim 180\mu W$

*Excludes power consumption of the integrated heater

†N/R - Not reported

As can be seen from table 2.1, the proposed reference search algorithm has the highest ease of integration and consumes the lowest power. In the next section, we would look at developing a model to accurately access the tuning power and speed efficiency of tuning techniques.

3. TUNING EFFICIENCY MODELING*

Silicon photonics is particularly promising because of the emergence of techniques that allow for hybrid integration with silicon chips [39–43] and the potential to build densed WDM systems that allow for high IO counts. However, as discussed in Section 2, microring non-idealities require tuning of resonant wavelengths to achieve better performance. We have already discussed tuning controls and algorithms used in conditioning the resonance wavelength of ring resonators. In this section, we would focus on resonant wavelength stabilization techniques. A comparative study of existing and proposed tuning methods is discussed and efficiency modelling results are presented.

3.1 Tuning Schemes

When the ring modulator's resonance wavelength is not accurately aligned to the input laser wavelength, the result is an undesirable modulation depth. This is clearly illustrated in Fig. 3.1, resonance wavelength tuning is therefore necessary to stabilize the ring resonance to make up for any drifts that may have occured by virtue of fabrication tolerances and temperature variations.

There are several ways by which the resonant wavelength of a MR can be tuned. As identified earlier, effective index δn_{eff} variations account for most variations in the resonant wavelength. Hence the primary approach to tuning will be to change the effective index of the microring.

The effective index can be changed in a number of ways [3], these include the use

*Part of this section is reprinted with permission, from A. Titriku, C. Li, A. Shafik, and S. Palermo, "Efficiency Modeling of Tuning Techniques for Silicon Carrier Injection Ring Resonators," *IEEE Optical Interconnects Conference*, May 2014.

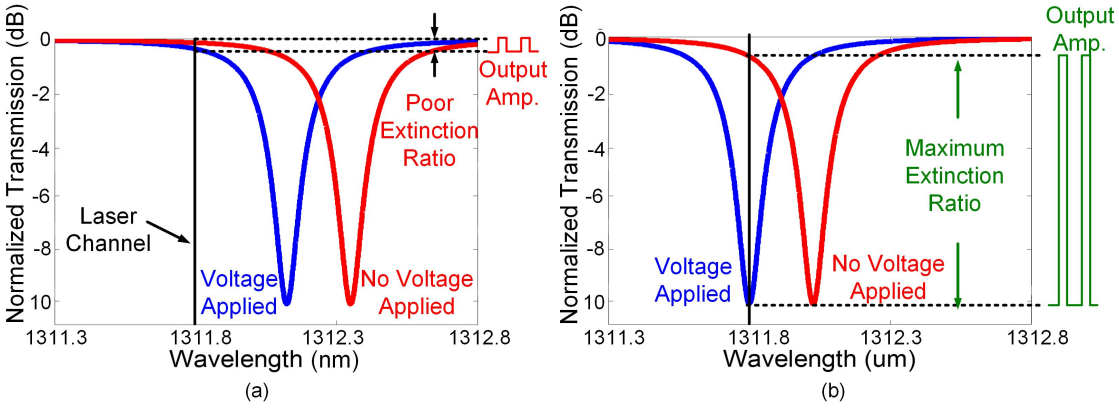

Figure 3.1: MR transmission curves showing extinction ratio when the resonance wavelength is (a) not properly aligned and (b) aligned with input laser wavelength [4]

of light via opto-optical effect [44], the use of an electric field (electro-optic effect) [45], the pumping of free carriers (carrier injection) [46, 47] and the application of heat to the ring (thermo-optic effect) [48]. The two common tuning methods considered are thermal and carrier injection (bias) tuning.

3.1.1 Thermal Tuning

Thermal tuning is achieved by varying the current through an integrated heater near the ring resonator, causing an increase in the refractive index of the silicon and the resonant wavelength to red shift (increased wavelength).

By the thermo-optic effect, the change in refractive index of a material can be as a result of a change in temperature and a change in density. The change in effective index with temperature is given as

$$\frac{dn}{dT} = -\left(\frac{\rho\delta n}{\delta\rho}\right)_T \gamma + \left(\frac{\delta n}{\delta T}\right)_\rho \tag{3.1}$$

where ρ is the density of the material and γ is the coefficient of volume expansion of the material.

A major advantage of thermal tuning is its potential to cover a wider temperature tuning range. However due to the poor tuning efficiencies of integrated heaters, thermal tuning typically consumes more power and is slower due to large thermal time constants.

Integrated heaters can be categorized into three groups silicon heaters and metal heaters with and without undercuts. Silicon ring heaters exhibit rather poor tuning efficiencies in the region of $42\mu W/GHz$ [49]. To improve the tuning efficiency of integrated heaters, thermal isolation of the resonance structure from the silicon substrate is one method that is employed. Undercut metal heater structures are realized by etching away localized silicon substrate during post processing. This reduces the thermal impedance by a factor of 24 translating to an order-of-magnitude reduction in tuning power [21, 27]. Adiabatic microring resonators have been proposed having the benefits of allowing interior connections to the resonator while suppressing spurious optical modes and maintaining a small footprint [50].

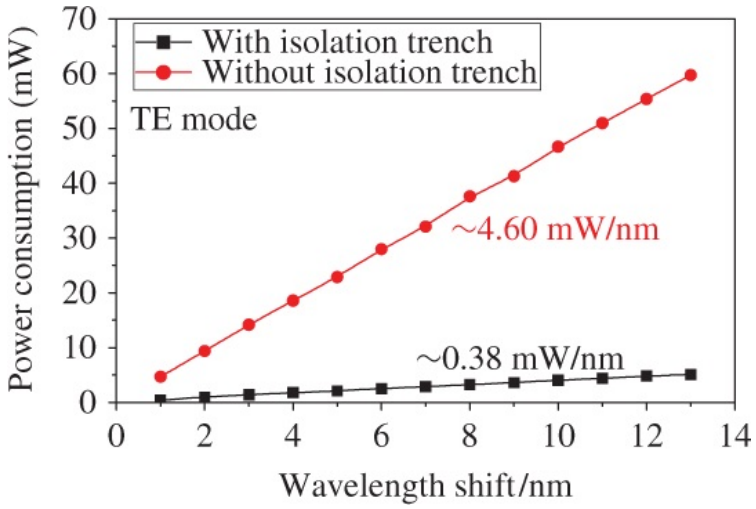

Figure 3.2: Tuning power of both of tunable filters with and without isolation [11]

There exists an inherent trade-off between tuning power and speed for integrated heaters with thermal isolation trenches. Fang *et. al* in their work [11] illustrated that although there was $\sim$ 12X improvement in tuning power with isolation, the 10%-90% rise time was $\sim$ 28X worse as shown in Figs. 3.2 and 3.3. While thermally isolated structures have been demonstrated to achieve very superior tuning efficiencies as low as $1.7\mu W/GHz$, it comes at the expense of tuning speed with thermal time constants as high as $\sim$ $170\mu s$ [21]. Aside speed and complication in fabrication, another potential problem with undercut structures is thermal crosstalk between adjacent heaters [27].

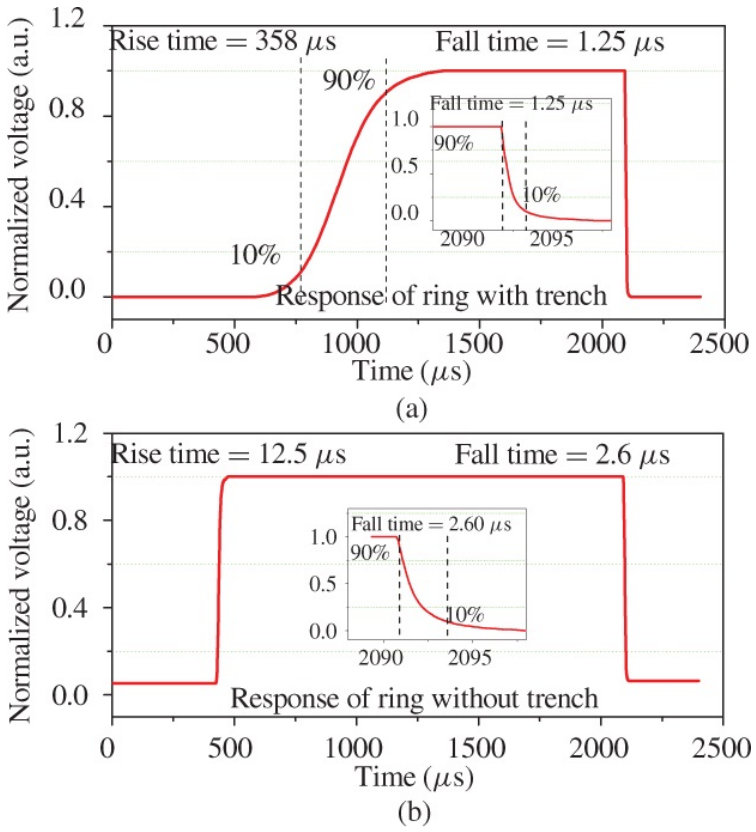

Figure 3.3: Temperature-rise response of tunable filter (a) with and (b) without isolation [11]

Moreover, it must also be noted that increasing the thermal impedance of the MR will increase it's susceptibility to various optical bistability effects, which can have undesirable effects on its modulation [35, 51].

3.1.2 Bias Tuning

Bias tuning involves varying the DC forward-bias current that is applied to the ring modulator. By changing the carrier density, the effective refractive index decreases and ultimately blue-shifts the resonant wavelength. Fig. 3.4 shows the change in resonance wavelength as the anode voltage of the resonator diode is increased.

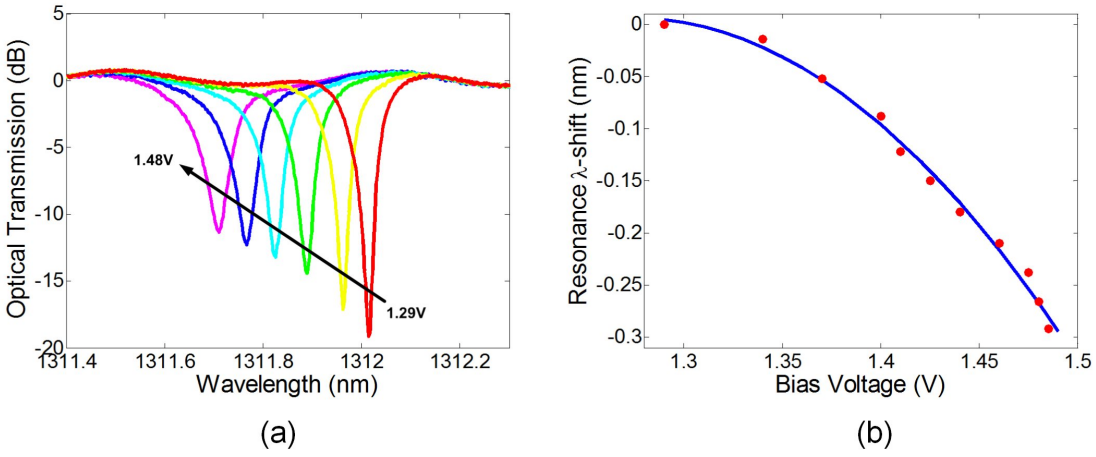

Figure 3.4: (a) Transmission spectra of carrier-injection MR at different bias levels (b) resonance wavelength shift versus bias voltage [4]

This provides the flexibility and the potential for a very fast tuning mechanism [4, 52]. Although this is an effectively fast and low power tuning method, it comes with the disadvantage of having a limited tuning range, some optical loss and reduction in quality factor. Another limitation of bias tuning is its availability and effectiveness to only carrier-injection based MR modulators.

3.1.3 Dual-loop Tuning

A hybrid tuning technique, denoted as dual-loop tuning involves a smart mix of bias and thermal tuning to take advantage of the thermal tuning large range and the bias tuning fast speed. Two dual-loop tuning approaches are proposed. The first simple approach illustrated in Fig. 3.5(a) involves starting the tuning with the bias loop and relinquishing control to a fine resolution thermal loop to complete the tuning if the bias loop is not successful. This allows for rapid tuning within the bias loop range and minimum power consumption when the thermal tuning is activated. The second coarse-fine method (Fig. 3.5(b)) involves taking coarse thermal steps equal to the bias tuning range and fine tuning with bias until a successful lock is achieved. This allows for a dramatic increase in tuning speed with even large variations, at the cost of some power overhead due to the flexibility of the simple dual-loop to tune negative mismatches.

3.1.3.1 Simple Dual-loop Tuning

A walk through the simple dual-loop tuning process as illustrated in Fig. 3.6, starts with bias tuning, and when lock fails, the thermal loop is activated to finish the tuning process. This allows for rapid tuning within the bias range using bias tuning. It also has the potential for low power consumption since there is no power overhead when the thermal loop is active. However, this tends to be slower due to the slow speed of the thermal control for fine resolution.

3.1.3.2 Coarse-fine Dual-loop Tuning

As mentioned earlier, the coarse-fine dual-loop tuning utilizes both bias and thermal schemes systematically. The process starts with a bias search, when lock is not achieved, the thermal loop steps up by a magnitude equivalent to the bias tuning

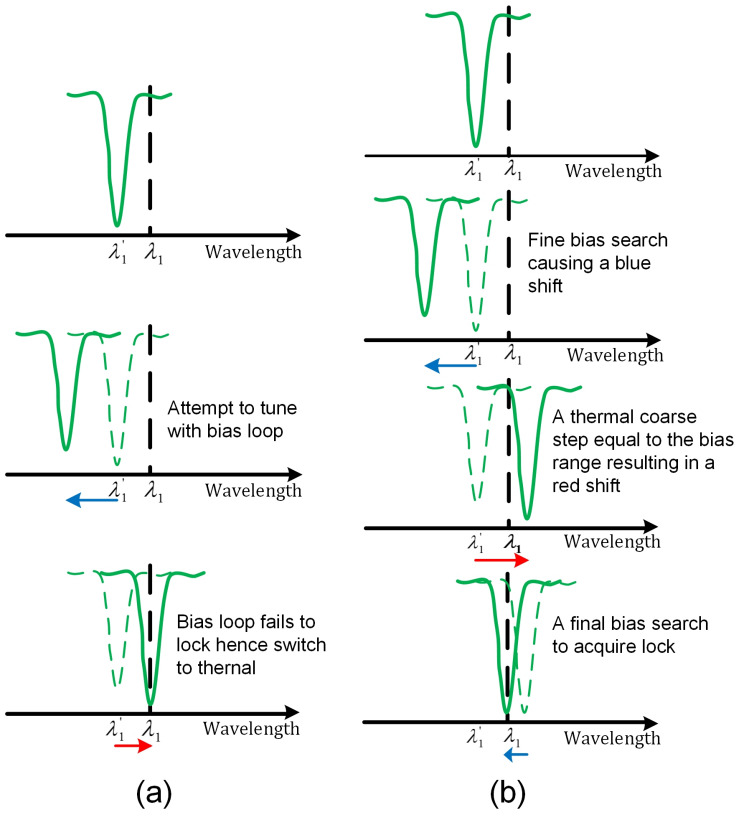

Figure 3.5: (a) Simple and (b) coarse-fine dual-loop tuning approaches

range. After the step, the bias loop is engaged again to fine search. This continues till lock is achieved. This technique allows for a dramatic speed increase due to coarse thermal steps, note the 5x smaller time axis in Fig. 3.7. The downside though is the potential for more power consumption due to the relative tuning efficiency of both loops.

3.2 Tuning Efficiency Model

In order to evaluate the tuning power efficiency and speed of the aforementioned wavelength stabilization techniques, a Matlab-based tuning model is developed. WDM systems employing between $5 - 20$ rings with a 3.7THz free spectral range (FSR) are modeled. These rings are designed with an 80GHz channel spacing

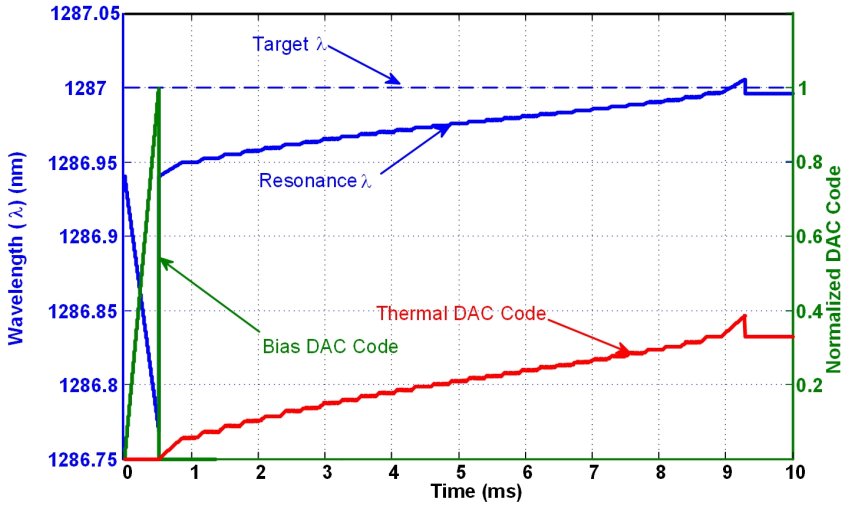

Figure 3.6: Simulation result illustrating simple dual-loop tuning

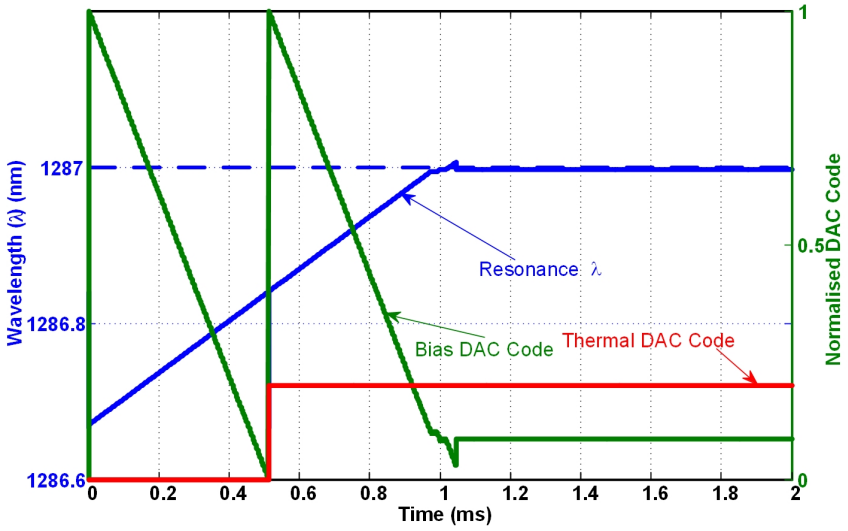

Figure 3.7: Simulation result illustrating coarse-fine dual-loop tuning

to match an assumed comb laser source. In lieu of tuning a specific ring to an assigned wavelength, ring shuffling is employed to allow tuning to the nearest available wavelength [16]. This is depicted in Fig. 3.8. The bias tuning is modelled with a $6.8\mu W/GHz$ efficiency and 0.28nm range, while the thermal tuning is assumed to

have $10\mu W/GHz$, a $77\mu s$ time constant, and sufficient tuning range to cover $5nm_{rms}$ variation. Table 3.1 summarizes the parameters used in the modelling analysis.

Table 3.1: Tuning model parameters

Parameter	**Value**
Free Spectral Range (FSR)	3.7 THz [21]
Channel Spacing	80 GHz
Bias Tuning Efficiency	6.8 μW/GHz [53]
Thermal Tuning Efficiency	10 μW/GHz [17]
Thermal Time Constant	77 μs [21]
Bias Tuning Range	0.28 nm [53]
Data Rate per Channel	10 Gb/s
Number of Runs	1000
Photonic Ring Type	Carrier injection

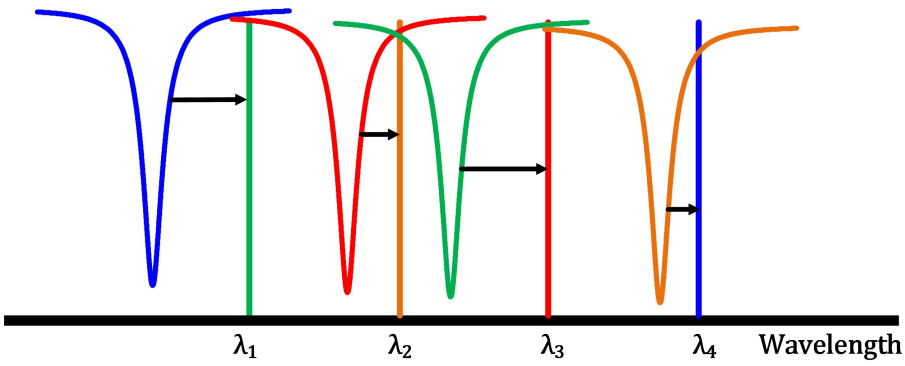

Figure 3.8: Ring re-shuffling

To begin with, a set of carrier-injection microring resonators with desired resonances and fabrication tolerances are assumed. Random wavelength shifts are added to the resonance wavelength. A statistical distribution of the wavelength drift is

shown in Fig. 3.9. The optical source assumed is a comb laser with 80 GHz channel spacing. Each ring is tuned to the closest available laser channel and when successful the tuning power and tuning speed is calculated. The average tuning power and speed over a 1000 Monte Carlo runs is then reported. The results are discussed below.

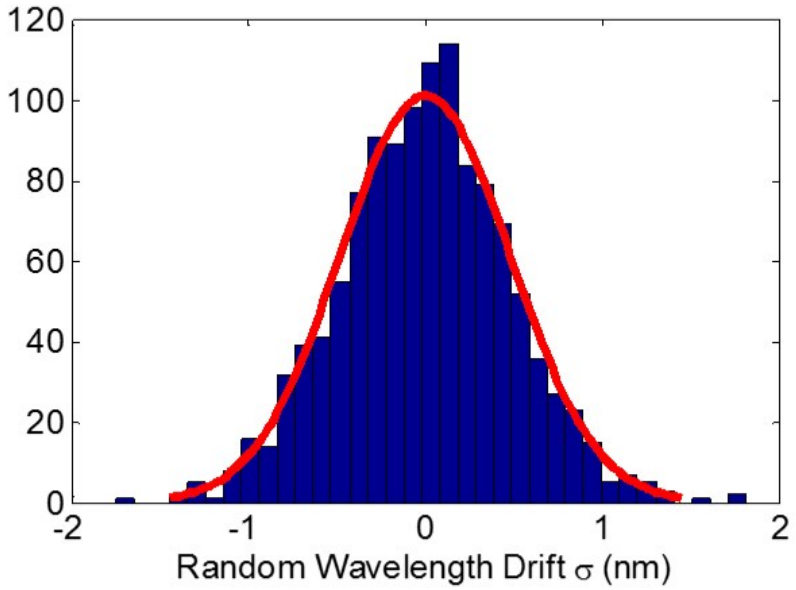

Figure 3.9: Distribution of λ mismatch for one ring

As shown in the tuning power versus wavelength mismatch results of Fig. 3.10, thermal tuning consumes the most power for smaller mismatch standard deviations ($< 2.5nm$), with 33% and 12% more power relative to the simple and coarse-fine dual-loop tuning, respectively, for a 20 ring system with $1nm_{rms}$. The simple dual-loop records the lowest power in that region. The coarse-fine dual loop tuning consumes more power than the simple dual-loop tuning. This power overhead (Fig. 3.11) can be attributed to the flexibility of the simple dual-loop to tune negative mismatches.

With larger mismatches, all schemes display similar performance due to the thermal tuning power dominating.

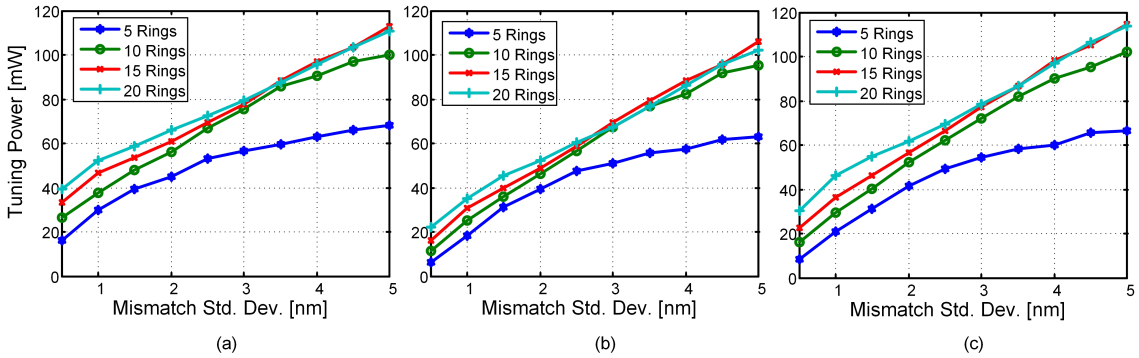

Figure 3.10: Tuning power for (a) thermal tuning (b) simple dual-loop tuning and (c) coarse-fine dual-loop tuning

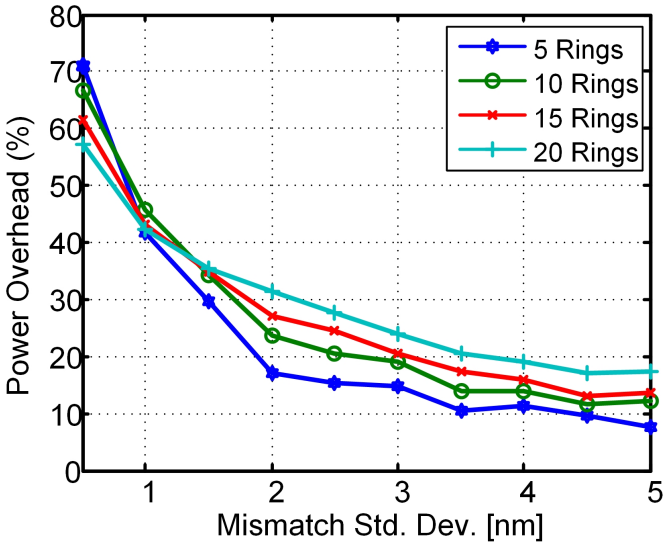

Figure 3.11: Coarse-fine/simple dual-loop tuning power overhead

It is also observed that the tuning power for all three techniques scales linearly with the thermal tuning efficiency as can be seen in Fig. 3.12. As integrated ring heater technologies are advancing, post processing techniques such as undercutting will make for lower thermal tuning efficiencies which will translate to lower power.

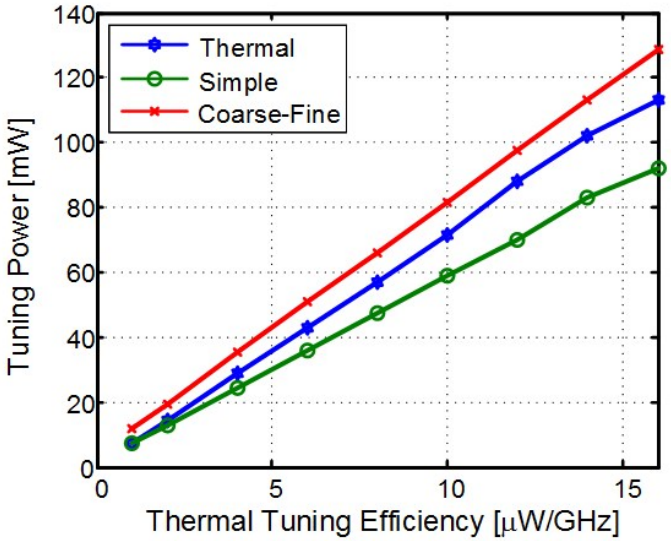

Figure 3.12: Tuning power for 20 rings at $2.5nm_{rms}$

The simple dual-loop tuning records similar numbers to the thermal tuning in terms of speed due to a single bias sweep followed by thermal tuning. The spread in the curves of the simple dual-loop is because more thermal tuning needs to be done for fine resolution. The potential of the coarse-fine dual-loop technique is highlighted in the Fig. 3.13 tuning speed results, with as much as a 16X improvement (Fig. 3.14) in speed observed at the same resolution due to the fine tuning achieved with the high-speed bias tuning. Due to only a single bias sweep with the simple dual-loop approach, its tuning speed is similar to thermal-only tuning.

The tuning speed depends heavily on the thermal time constant. Smaller thermal

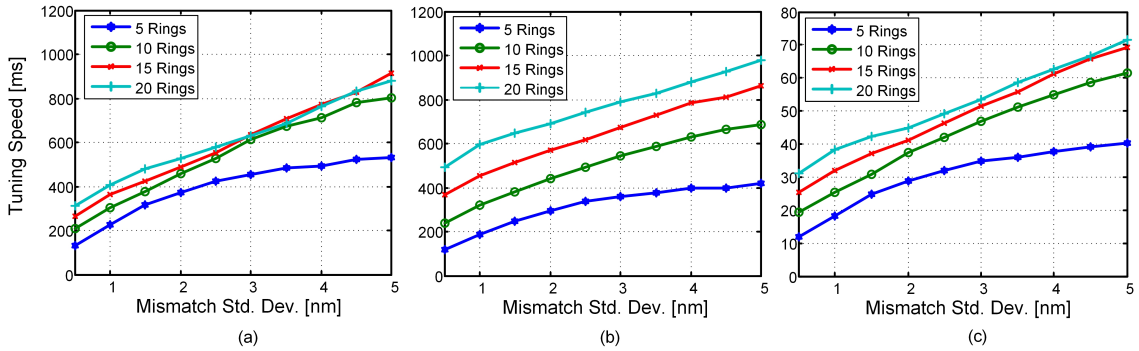

Figure 3.13: Tuning speed for (a) thermal tuning (b) simple dual-loop tuning and (c) coarse-fine dual-loop tuning

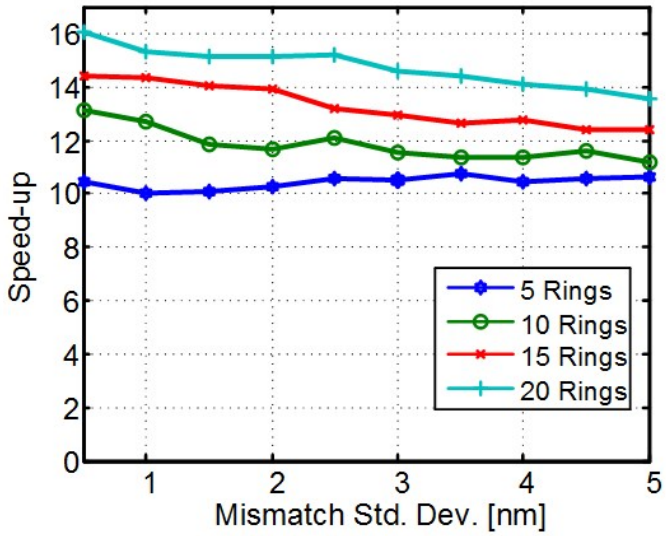

Figure 3.14: Coarse-fine/simple dual-loop tuning power speed-up

time constants will produce faster tuning times. As seen in Fig. 3.15, as the thermal time constant approaches the bias tuning time constant, all three methods record similar tuning speed numbers.

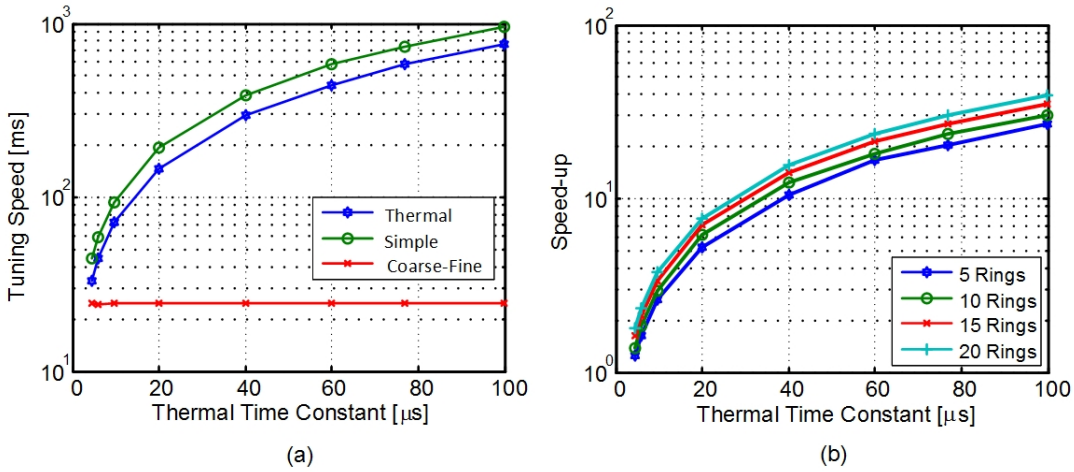

Figure 3.15: (a) Tuning speed vs thermal time constant for 20 rings at $2.5nm_{rms}$ (b) Coarse-fine/simple dual-loop tuning power speed-up vs thermal time constant

3.3 Summary

The importance of resonance wavelength stabilization schemes cannot be overemphasized in silicon photonics and optical links for that matter. This section examined the different types of tuning methods available.

The proposed dual-loop tuning approach discussed in this section is seen to have superior tuning efficiency metrics compared to traditional thermal only tuning. It is evident from the modelling results obtained that, dual-loop tuning scheme allows for dramatic improvements in power efficiency with small variations and tuning speed over a wide variation range, providing the potential for rapid tuning of large ring count systems with minimal power overhead.

4. SILICON RING RESONATOR TUNING IMPLEMENTATION

The design objectives for the various blocks that comprise the tuning loop shown in Fig. 2.13 depend strongly on the specific function of the block. The ultimate goal is to design circuits that consume the least power and occupy as small an area as possible. This section looks at the circuit implementation of the various blocks shown in the tuning block diagram. Measurement results from both transmitter and receiver tuning implementations are also presented and discussed.

4.1 Tuning Blocks Design

4.1.1 Reference DAC

The reference DAC as the name suggests is used to generate the reference voltage used in the reference search tuning algorithm. It is a resistor ladder DAC with 6-bit control. As can be seen in Fig. 4.1, the three least significant bits (LSBs) are decoded into 8 bits and used to control the column of the ladder. In similar fashion, the three most significant bits (MSBs) are also decoded into 8 bits and used to control the rows. There is unity gain buffer at the output of the DAC to provide drive capability.

The DAC comprises $1k\Omega$ resistors connected in series that effectively divide the supply voltage into 2^6 equal voltages. Using the right selection of row and column bit controls, the corresponding voltage to an input bit combination is tapped to the input of the unity gain buffer which is then copied to the output. Fig. 4.2 shows the stair case transfer characteristics of the reference DAC.

4.1.2 Thermal DAC

The thermal DAC is a current DAC. The thermal control from the tuning FSM is a 12-bit word. The 8 LSBs are resolved into a 1-bit sigma-delta control. Hence

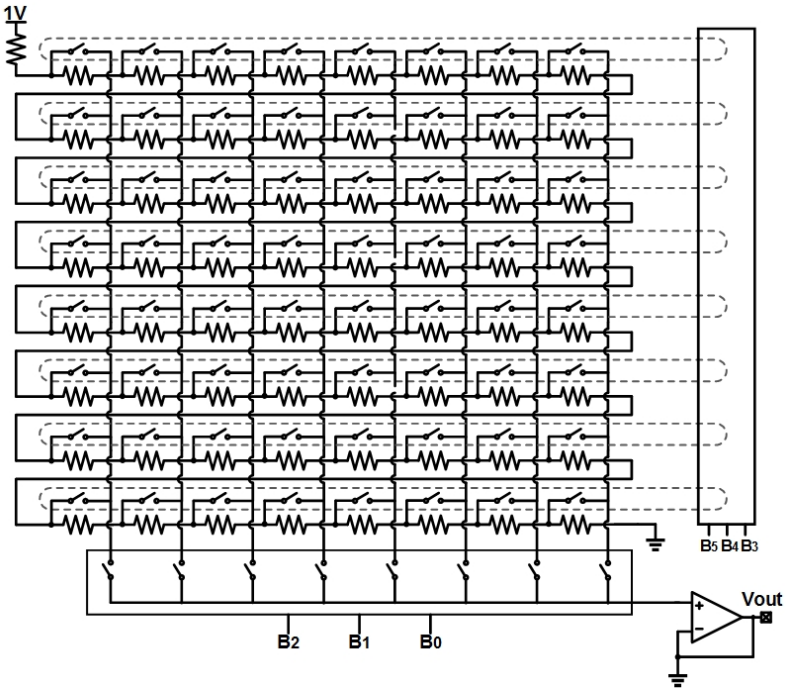

Figure 4.1: Reference DAC

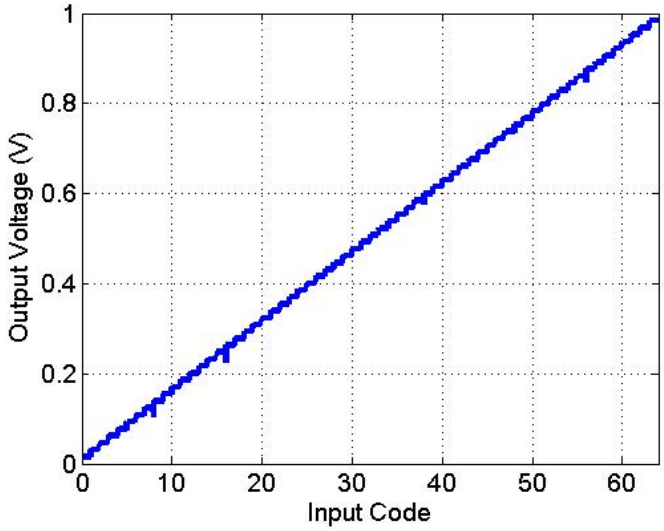

Figure 4.2: Reference DAC transfer characteristics

the thermal DAC itself is a 5-bit input DAC as illustrated in Fig. 4.3.

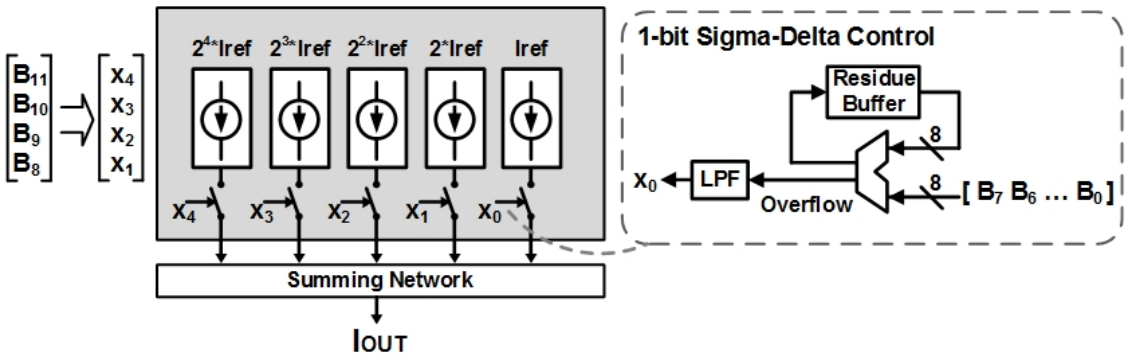

Figure 4.3: Thermal DAC with sigma-delta control

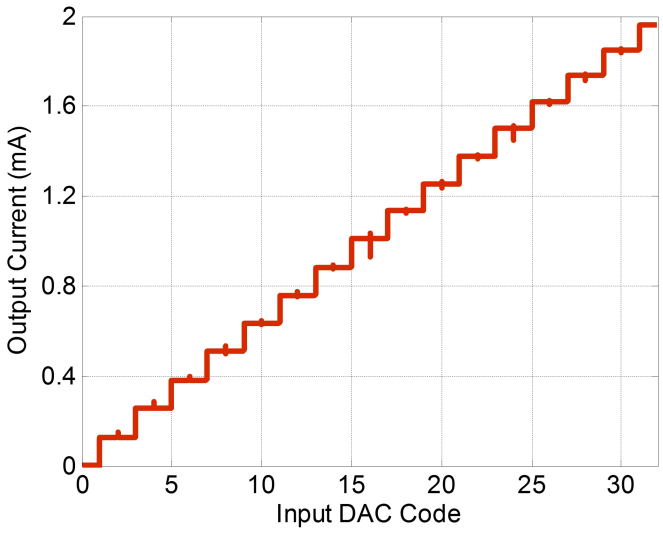

Figure 4.4: Thermal DAC transfer characteristics

The 4 MSBs provide course steps and the 1-bit sigma-delta control enables some sort of fine step capability. With a reference current, each ith branch produces

current which is 2^i times the reference current. The currents are summed up and delivered to the integrated heater. Fig. 4.4 shows the output current curve of the thermal DAC with a linear input binary ramp.

4.1.3 Current-injection (Bias) DAC

In order to linearize the bias control, the bias DAC is designed to have a nonlinear response that counteracts the nonlinear I-V characteristics of the ring diode device. The DAC comprises a 3-bit segmented nonlinear DAC which forms the MSB control and a 6-bit linear R-2R DAC making the LSB control. This yields an effective 9-bit nonlinear voltage DAC. Fig. 4.5 shows the schematic diagram of the bias DAC. The bias DAC also has a unity gain buffer at its output to provide drive strength.

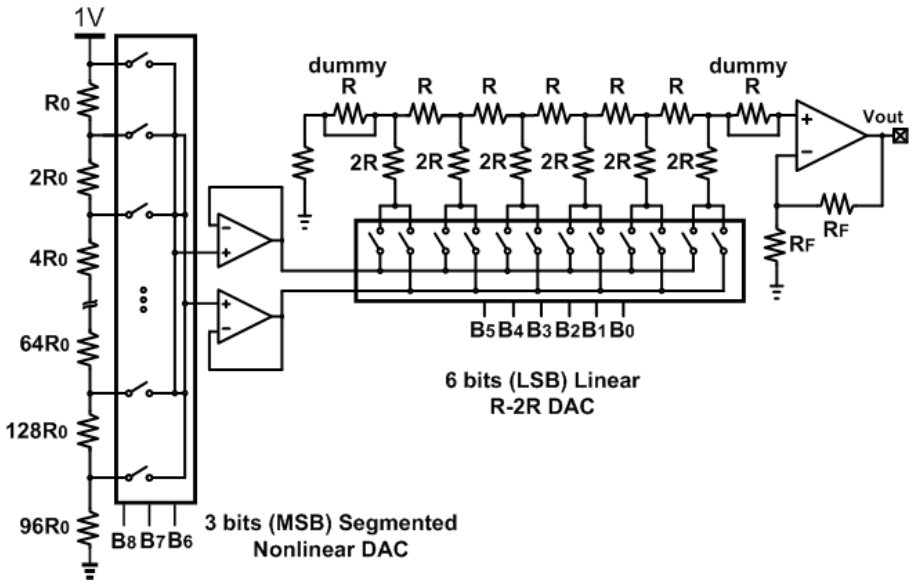

Figure 4.5: Current-injection DAC [4]

The non-linear transfer curve of the DAC is presented in Fig. 4.6.

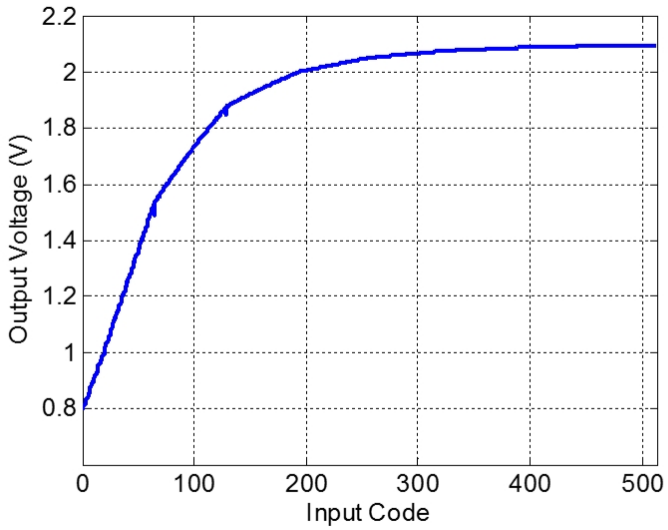

Figure 4.6: Current-injection DAC transfer characteristics

4.1.4 TIA

In transmitter side tuning, a low bandwidth TIA such as a tunable resistor (Fig. 4.7) is used to convert the current from the monitor PD into voltage for the comparator input.

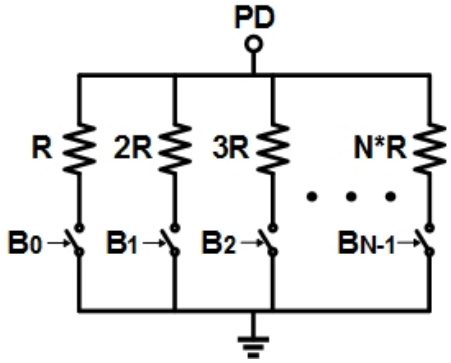

Figure 4.7: TIA

4.1.5 Peak Detector

It is common place for most TIAs employed in high speed receivers to have some form of offset-correction feedback. This makes it difficult to tune to the average optical power in dynamic mode. Hence for receiver side tuning, a peak detector shown in Fig. 4.8 is placed after the TIA to sense the peak power which is then compared with the reference to decide in which direction to tune the ring. The peak detector is reset by a delayed version of the comparator clock.

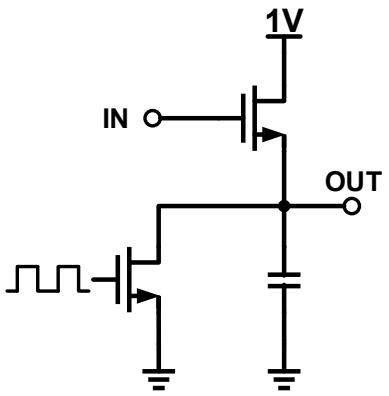

Figure 4.8: Peak detector

4.1.6 Comparator

The dynamic comparator used for the tuning loop is the double tail voltage sense amplifier by Schinkel *et. al* in [12]. As shown in Fig. 4.9, the Schinkel latch has less stacking than the conventional latch hence allows for low voltage operation. Furthermore, the double tail configuration enables input and latch stage currents to be independently set, this reduces offset.

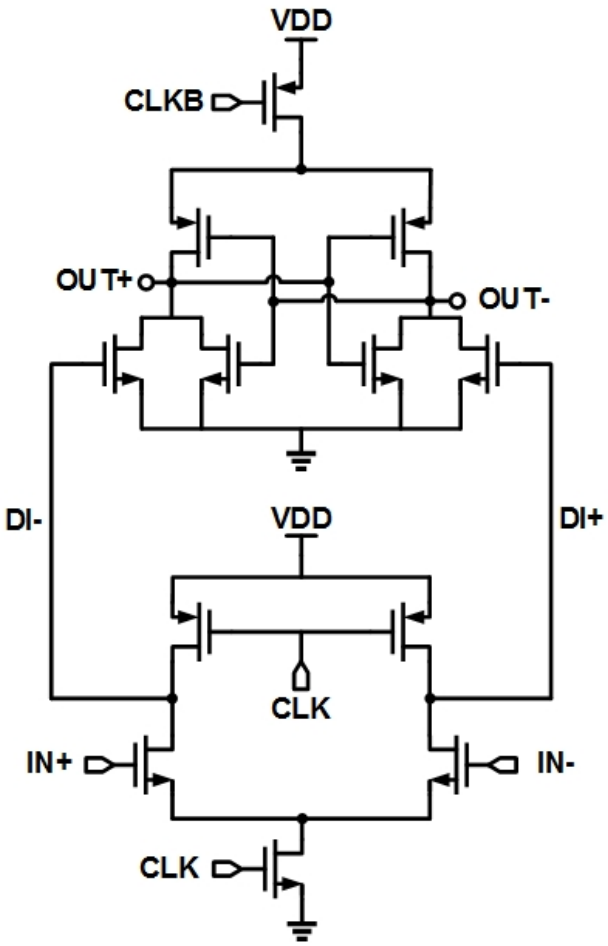

Figure 4.9: Low voltage Schinkel sense amplifier [12]

However, the comparator requires complementary clock signals. This makes it sensitive to skew. A current DAC is therefore used to control the offset in both arms of the input stage. The sense amplifier is followed by a conventional SR latch shown in Fig. 4.10.

4.1.7 FSM

The digital FSM is used to control the tuning process of the rings. It takes the comparator output and averages it to decide wither to increase or decrease the tuning DACs in order to achieve lock. To do the averaging, two 18-bit thresholds -

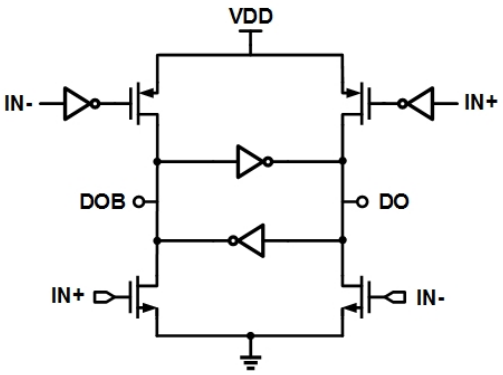

Figure 4.10: SR latch

TH1 and TH2 - which can be controlled dynamically are used. When the number of comparator '1's is greater than TH1, the tuning DACs are increased. The converse occurs when the number of comparator '1's is less than TH2. Two different thresholds are defined to make for random noise in the system. Once an initial lock is achieved, which means that the power level at the ring output is equal to the initial reference voltage level, the FSM steps up the reference level, and tries to re-achieve lock by changing the tuning DAC code. The step is repeated until the maximum output power at the drop port is reached, which means that the ring has been successfully tuned. The FSM can be programmed to operate in either through port or drop port mode by setting the appropriate control bits.

When used in a WDM system, the FSM operates based on a time division multiplexing principle. Rings are tuned systematically from the closest to the input laser source to the farthest. However, at the cost of increased area, the FSM can be extended to simultaneously tune all channels at the same time by doing a dedicated averaging for each channel. The FSM logic was implemented using verilog and the optimized code was synthesized in the 65nm CMOS technology. The synthesized layout shown in Fig. 4.11 occupies an area of $13.2nm^2$.

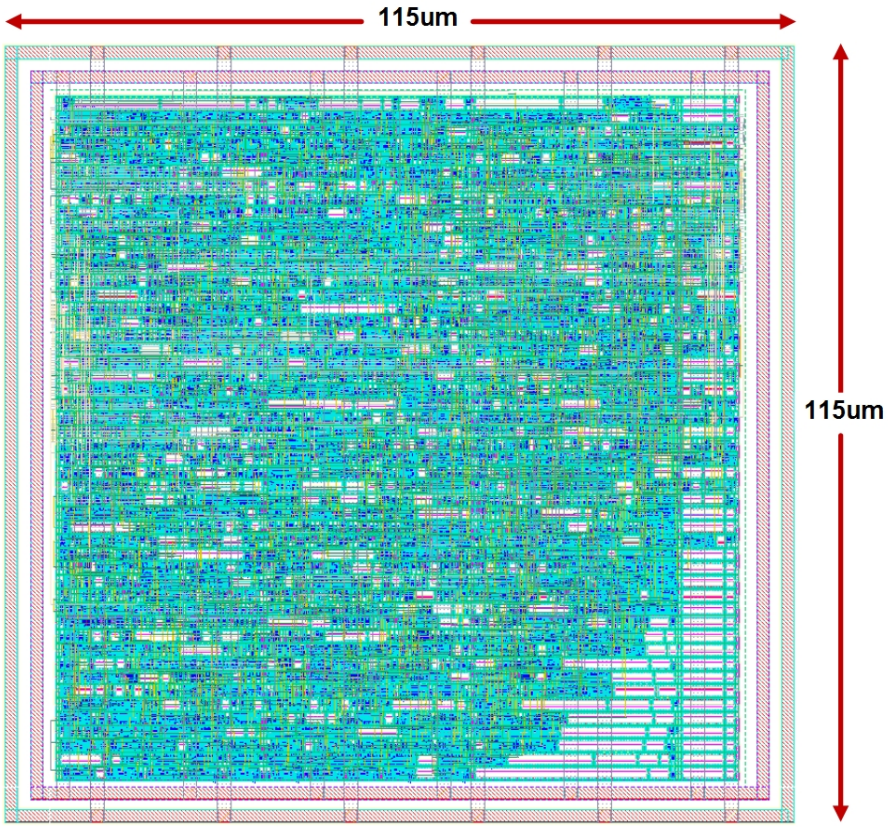

Figure 4.11: Synthesized FSM layout

4.2 Transmiter Tuning Implementation

The transmit-side tuning was implemented in two versions; the first version used pulse width modulation (PWM) for the thermal control whereas in the second version, the thermal control was executed using sigma-delta modulation (SDM).

PWM generates a square wave whose symmetry is controlled in linear fashion by an input signal compared with a slowly varying triangular or saw-tooth wave. As seen in Fig. 4.12, for the same number of bits, SDM produces far less ripples than PWM due to its noise shaping characteristics. Using SDM therefore will reduce the amplitude of ripple noise on the output of the thermal DAC. This can be attributed

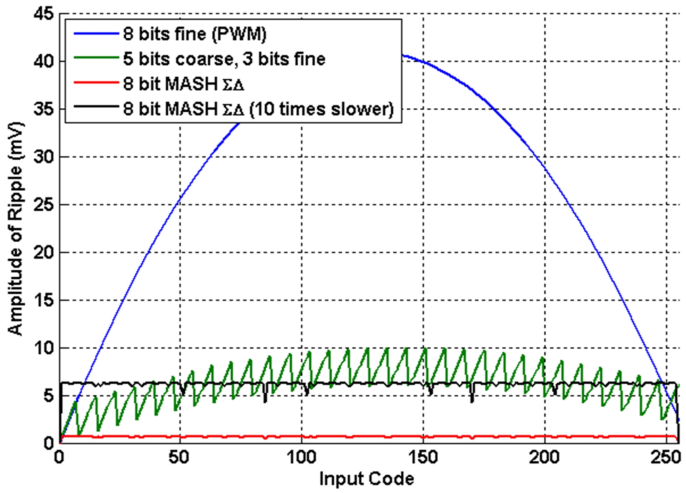

Figure 4.12: PWM vs SDM comparison

to the noise shaping characteristics of the SDM.

For the transmitter side tuning, the through port of the MR was monitored using a monitor PD and using a low-bandwidth tunable resistor TIA, the input current was converted into voltage which was compared with a predefined reference.

Figs. 4.13 and 4.14 show Cadence simulation results verifying the functionality of the transmit-side static tuning loop. Starting at an initial high value, the MR output power reduces gradually as the reference DAC steps down to find the optimal minimum point that will yield maximum extinction ratio. In like fashion, the thermal DAC output current reduces as the reference DAC steps down. Note that the error between the final reference DAC value and the ring output power is due to the finite loop gain of the tuning loop.

4.2.1 Experimental Results

Version 1

In the first version IC, carrier-injection ring modulators were used for the photonic IC.

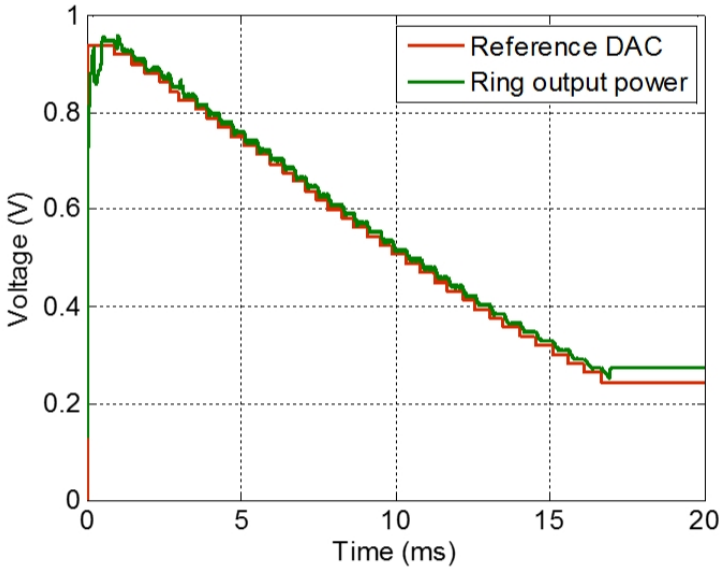

Figure 4.13: Transmitter through port tuning simulation result

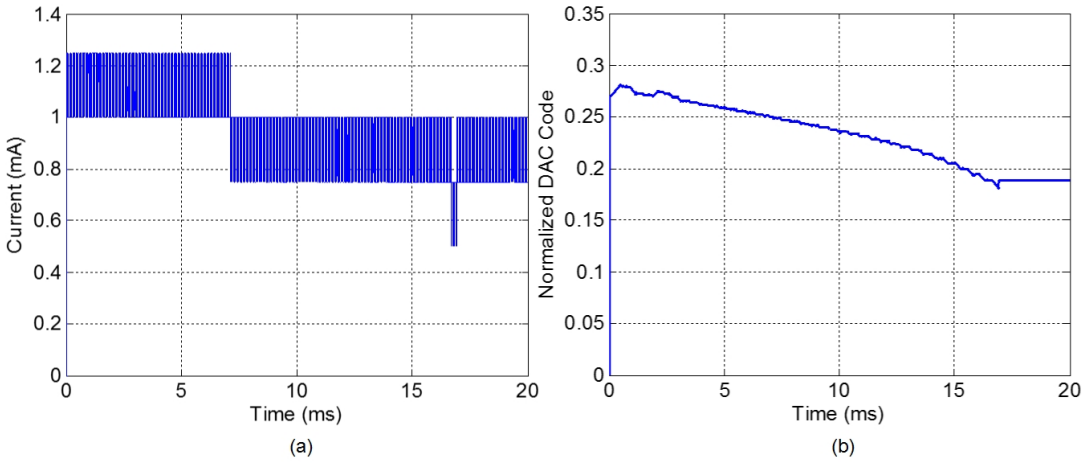

Figure 4.14: Simulated thermal DAC (a) current and (b) averaged output in TX through port tuning

The ring heater with a sheet resistance of 800Ω/□ was realized by doping the silicon at the same step as the p-i-n junction formation. Since carrier-injection modulators

were used, it was possible to implement both bias and thermal based tuning.

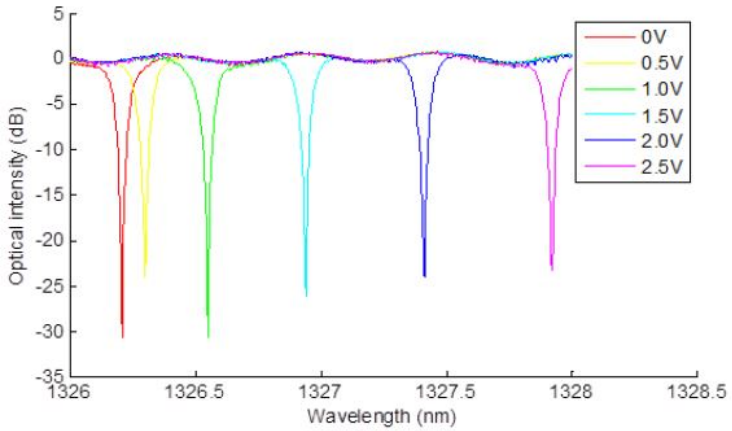

Figure 4.15: Ring output spectra for various heater biases

The measured resonance wavelength drifts as the ring heater bias was varied is presented in Fig. 4.15. A tuning efficiency of $23\mu W/GHz$ was obtained. Fig. 4.16 shows a high speed more energy efficient fine bias tuning. The tuning range measured was $0.3nm$ with a tuning efficiency of $6.8\mu W/GHz$.

Version 2

The second version of the TX used depletion mode ring modulators with a radius of $7.5\mu m$ and a Q-factor of ~ 5000. Bias based tuning is not efficient in depletion mode devices hence only thermal tuning was implemented. The ring heater had a resistance of $1k\Omega$. The static tuning was successfully demonstrated and presented in Fig. 4.17.

In order to verify the dynamic tuning operation of the loop, an adjacent ring resonator heater is modulated with a voltage ramp to cause some temperature fluctuations as shown in the block diagram in Fig. 4.18

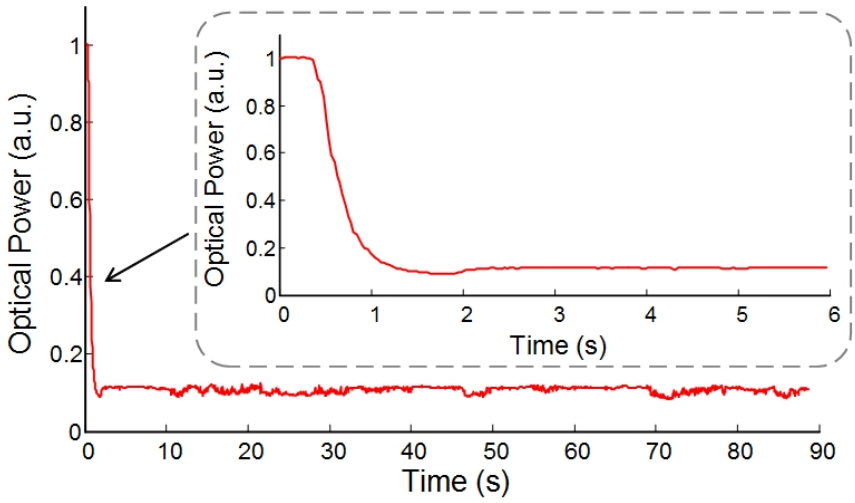

Figure 4.16: Optical output at through port during bias tuning

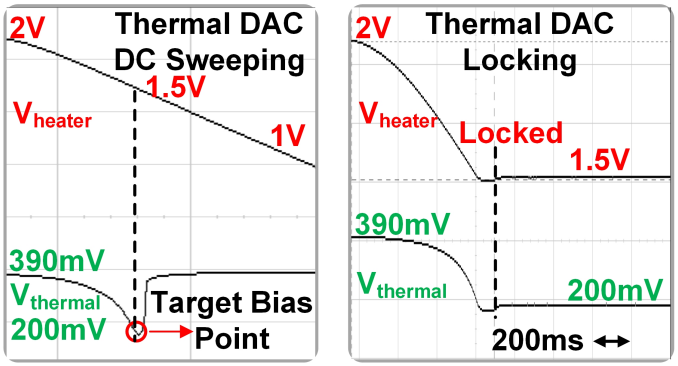

Figure 4.17: Static thermal tuning

With modulated data applied to the ring, it is observed that the optical eye opening suffers severely as the thermal tracking is disabled due to the effect of resonant wavelength shift. As seen in Fig. 4.19, a healthy optical eye opening is obtained when thermal tracking is enabled and the thermal fluctuations are suppressed.

With a 2V thermal DAC dynamic range, $\sim 0.8nm$ wavelength tuning range was achieved. The power breakdown for the tuning loop is summarized in table 4.1. This

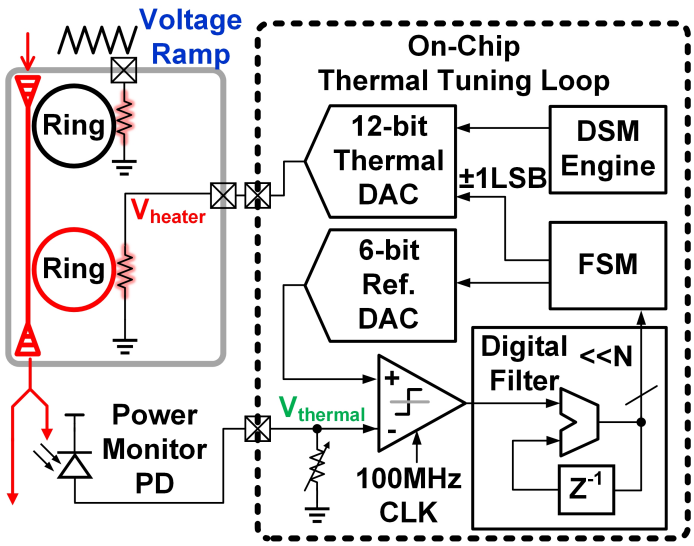

Figure 4.18: Dynamic thermal tuning block diagram

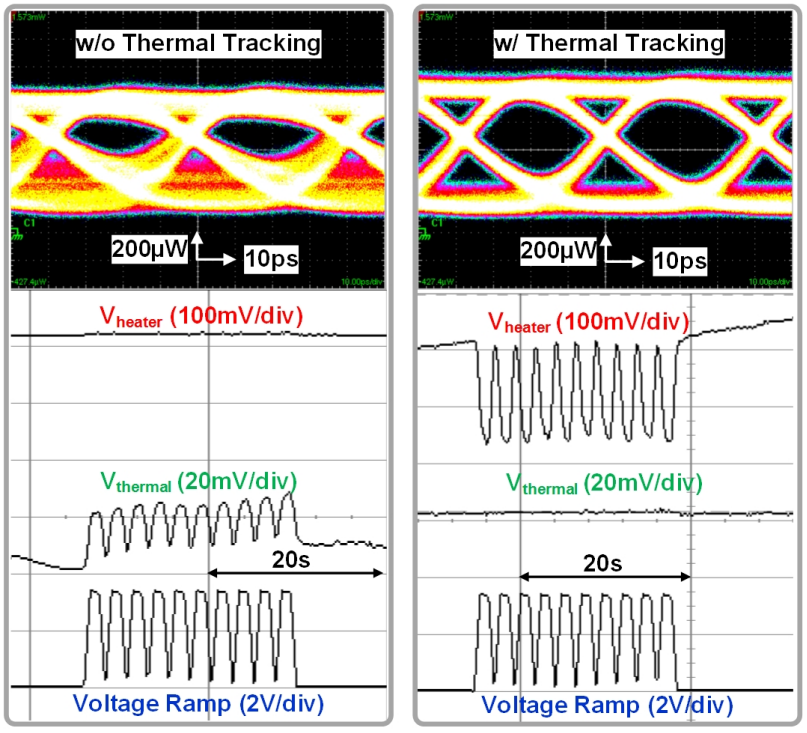

Figure 4.19: Dynamic thermal tracking

translates to a tuning efficiency of $51\mu W/GHz$.

Table 4.1: Thermal tuning power breakdown

Block	**Power**
Thermal DAC	$5mW$
FSM @ 100MHz	$150\mu W$
Comparator	$4.5\mu W$
Reference DAC	$18.7\mu W$
Total	$5.17mW$

4.3 Receiver Tuning Implementation

In implementing the receive-side tuning, the drop-port of the ring filter is monitored using a waveguide PD to ascertain if the ring resonance is precisely aligned with the input laser wavelength. Unlike the transmit-side tuning, due to the offset-correction feedback loop in the high-speed receiver TIA shown in Fig. 4.20, average-power-based tuning is not feasible. A peak detector is therefore placed at the output of the TIA to sample the peak ring output power at a clock frequency of the FSM clock as shown in Fig. 4.21. Moreover, the RX FSM slightly differs from the TX FSM in that, it also monitors to see if there is actual modulation data on the channel before tuning commences.

Static drop-port tuning functionality was also verified via Cadence simulation. As shown in Figs. 4.22 and 4.23 , the optical ring output power increases as the reference voltage steps up until the optimal power that yields the maximum extinction ratio is reached.

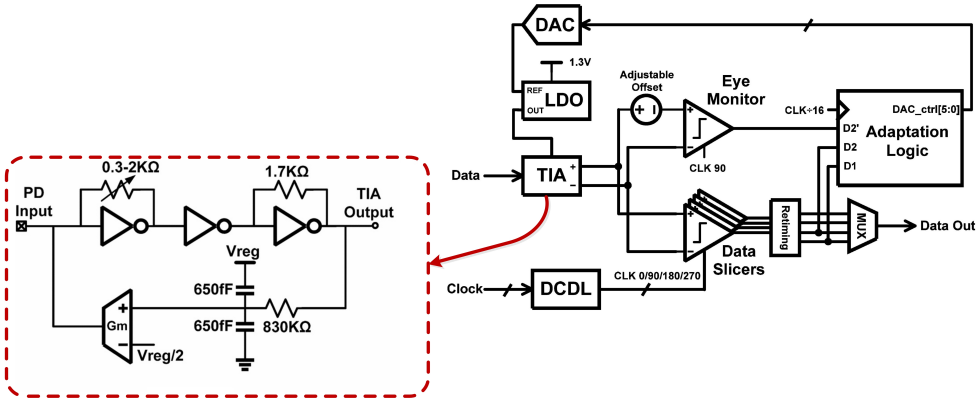

Figure 4.20: High speed receiver [4]

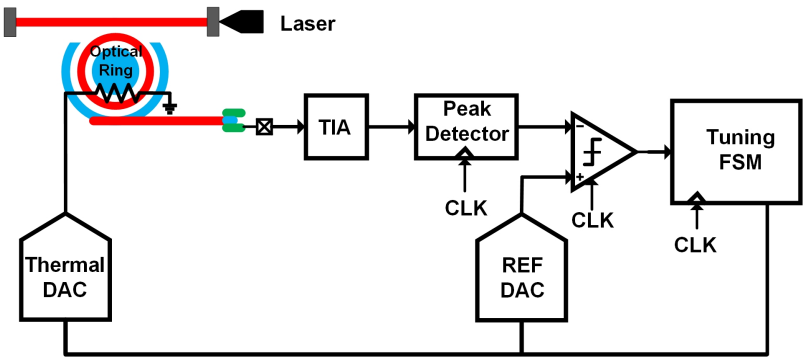

Figure 4.21: Receiver side tuning block diagram

4.3.1 Experimental Results

Using microring drop filters of radius $5\mu m$ and a Q-factor of $\sim$ 18000, the drop-port power was sampled using the peak detector to make a decision whereas through-port power was monitored using a power meter to verify the resonant wavelength stabilization.

Fig. 4.24(a) illustrates the measured drop filter through-port response at different thermal DAC current bias levels. A tuning range of $0.7nm$ is achieved over $2mA$ dynamic range of current. Fig. 4.24 verifies static receive-side drop-port tuning.

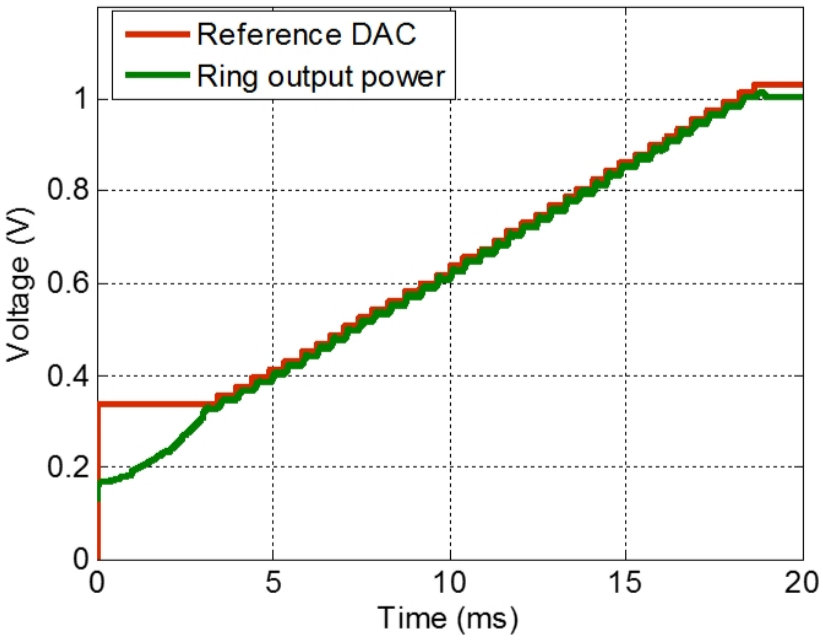

Figure 4.22: Simulated receiver drop-port static tuning

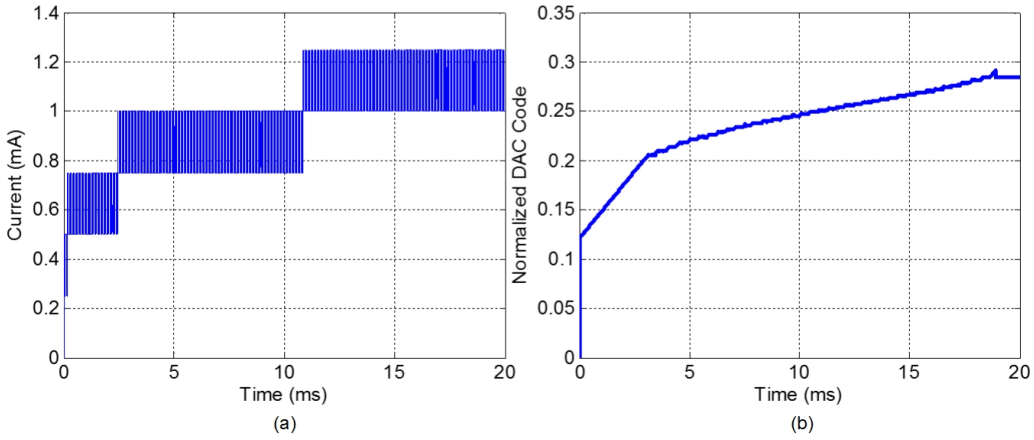

Figure 4.23: Simulated thermal DAC (a) current and (b) averaged output in RX drop-port tuning

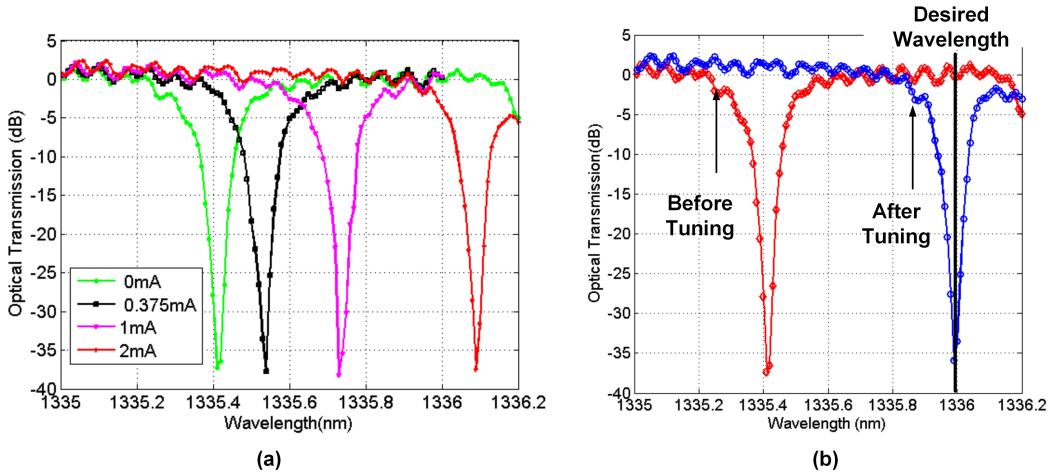

Figure 4.24: Measured MR drop filter spectra (a) at different thermal biases and (b) showing loop locking

The ring drop filter which is initialize at $1335.4nm$ is wavelength locked to $1336.0nm$ using the automatic tuning loop.

4.4 Summary

In this section we discussed the different circuit components used to implement the reference search based tuning algorithm in silicon. The key consideration in the design of the various blocks was low power and area consumption. Simulation results for the various blocks were shown to verify their correct operation.

The implementation of both transmit-side through port tuning and receive-side drop-port tuning were also described in this section. Our simulation and measurement results showed that the loop architecture operated according to design and achieved acceptable tuning ranges. Both static and dynamic tuning were succesfully demonstrated for the TX tuning. However only static tuning has yet been shown for the RX tuning. Table 4.2 summarizes the performance of the transceiver tuning as compared with recent state-of-the-art implementations. Further testing will be done

to demonstrate dynamic tuning for the receive-side.

Table 4.2: Comparison of tuning performance

	Liu [54] JSSC 2012	**Sun [55]** VLSI 2014	**This Work** TXv1	RX	TXv2
Technology	40nm CMOS	180nm CMOS	65nm CMOS		
Microring Type	Depletion	Depletion	Injection		Depletion
Data Rate (Gbps)	10	5	5		25
Tuning Scheme	Manual Thermal	Thermal	Dual-bias/ thermal	Static Thermal	Dynamic Thermal
Tuning Range (nm)	0.75	0.5	0.3 Bias 1.7 Thermal	0.7	0.8
Tuning Power (mW)	6.4	0.43 *	0.34 Bias 6.94 Thermal	4.0	5.17

*Excludes power consumption of the integrated heater

5. CONCLUSIONS

Optical interconnects proffer an attractive alternative to mitigate I/O bandwidth limitations and frequency dependent channel loss issues in traditional high speed electrical interconnects. Silicon photonics is a key enabler of optical I/O technology. Silicon microrings with their small footprints and high contrast ratios form an integral part of silicon photonics. By leveraging CMOS monolithic integration technologies, it is conceivable that their ability to offer distance independent communication will lead to their commercial adoption in the near future.

However, resonance wavelength drifts are a major obstacle in the deployment of these high-Q devices in ring resonator based nanophotonic interconnects. This thesis has examined the sources and effects of microring non-idealities. The two major causes of resonance wavelength drift are identified as fabrication and manufacturing imperfections and dynamic drifts that arise from ambient temperature fluctuations. A study of existing resonance wavelength control algorithms was done.

The newly dual-bias/thermal tuning system presented in Section 3 based on the reference search algorithm is compared against conventional thermal tuning for carrier injection ring resonators using a statistical model. This dual-loop tuning scheme allows for dramatic improvements in power efficiency with small variations and tuning speed over a wide resonance wavelength mismatch variation range. It also provides the potential for rapid tuning of large rings count I/O systems with minimal power overhead.

The tuning loop was fabricated in GP 65nm CMOS technology in two versions of ICs. Both transmit-side tuning and receiver-side tuning were experimentally verified. The first version of the TX tuning which employed carrier-injection ring resonators

achieved a thermal tuning efficiency of $23\mu W/GHz$ over a tuning range of $\sim 1.7nm$ and bias tuning efficiency of $6.8\mu W/GHz$ across a $0.3nm$ tuning range. The second version of the TX used depletion mode microring modulators. As presented in Section 4, both static and dynamic tuning operations were demonstrated. The thermal only tuning consumed a total power of $5.17mW$ while convering a tuning range of $\sim 0.8nm$. The receiver side tuning was also verified experimentally for static tuning. A tuning range of $0.7nm$ was achieved over a $2mA$ dynamic range of current.

Going forward, the commercial use of optical I/O will majorly be dependent on the ability of high speed electrical I/O to scale and meet bandwidth and loss requirements of next generation communication links. Area, power and economic cost will ultimately be deciding factors in the adoption of silicon photonic technology.

5.1 Future Work

Future work to be done involves demonstrating dynamic tuning mode with modulated data for receive-side tuning. The course-fine dual loop tuning approach is yet to be implemented in silicon. This also has to be done to verify modeling results for speed and power efficiency. Finally, the FSM may be scaled to simultaneously stabilize the resonance wavelength of all channels.

REFERENCES

[1] G. T. Reed and A. P. Knights, *Silicon photonics: an introduction*. Chichester ; Hoboken, NJ: John Wiley & Sons, 2004.

[2] "File: Machzehnder.gif." http://photonicswiki.org/index.php?title=File:MachZehnder.gif. [Online: Accessed September-13-2014].

[3] D. H. Geuzebroek and A. Driessen, *Ring-resonator-based wavelength filters*, pp. 341–379. Berlin: Springer, 2006.

[4] L. Cheng, B. Rui, A. Shafik, E. Z. Tabasy, W. Binhao, T. Geng, M. Chao, C. Chin-Hui, P. Zhen, M. Fiorentino, R. G. Beausoleil, P. Chiang, and S. Palermo, "Silicon photonic transceiver circuits with microring resonator bias-based wavelength stabilization in 65 nm CMOS," *IEEE Journal of Solid-State Circuits*, vol. 49, no. 6, pp. 1419–1436, 2014.

[5] A. V. Krishnamoorthy, R. Ho, Z. Xuezhe, H. Schwetman, J. Lexau, P. Koka, L. Guoliang, I. Shubin, and J. E. Cunningham, "Computer systems based on silicon photonic interconnects," *Proceedings of the IEEE*, vol. 97, no. 7, pp. 1337–1361, 2009.

[6] C. Qiu, J. Shu, Z. Li, X. Zhang, and Q. Xu, "Wavelength tracking with thermally controlled silicon resonators," *Optics Express*, vol. 19, no. 6, pp. 5143–5148, 2011.

[7] E. Timurdogan, A. Biberman, D. C. Trotter, C. Sun, M. Moresco, V. Stojanovic, and M. R. Watts, "Automated wavelength recovery for

microring resonators," in *Conference on Lasers and Electro-Optics 2012*, OSA Technical Digest (online), p. CM2M.1, Optical Society of America.

[8] W. A. Zortman, A. L. Lentine, D. C. Trotter, and M. R. Watts, "Bit-error-rate monitoring for active wavelength control of resonant modulators," *IEEE Micro,*, vol. 33, no. 1, pp. 42–52, 2013.

[9] J. A. Cox, D. C. Trotter, and A. L. Starbuck, "Integrated control of silicon-photonic micro-resonator wavelength via balanced homodyne locking," in *IEEE Optical Interconnects Conference, 2013*, pp. 52–53.

[10] K. Padmaraju, D. F. Logan, T. Shiraishi, J. J. Ackert, A. P. Knights, and K. Bergman, "Wavelength locking and thermally stabilizing microring resonators using dithering signals," *Journal of Lightwave Technology*, vol. 32, no. 3, pp. 505–512, 2014.

[11] F. Qing, S. Junfeng, L. Xianshu, J. Lianxi, Y. Mingbin, L. Guoqiang, and L. Yuliang, "High efficiency ring-resonator filter with nisi heater," *IEEE Photonics Technology Letters*, vol. 24, no. 5, pp. 350–352, 2012.

[12] D. Schinkel, E. Mensink, E. Klumperink, E. Van Tuijl, and B. Nauta, "A double-tail latch-type voltage sense amplifier with 18ps setup+hold time," in *IEEE International Solid-State Circuits Conference (ISSCC) Digest of Technical Papers, 2007*, pp. 314–605.

[13] "International technology roadmap for semiconductors 2006 update," report, Semiconductor Industry Association (SIA), 2006.

[14] V. Stojanovic and M. Horowitz, "Modeling and analysis of high-speed links," in *IEEE Custom Integrated Circuits Conference, 2003, Proceedings*, pp. 589–594.

[15] L. Pavesi and G. Guillot, *Optical interconnects: the silicon approach*. New York: Springer, 2006.

[16] M. Georgas, J. Leu, B. Moss, S. Chen, and V. Stojanovic, "Addressing link-level design tradeoffs for integrated photonic interconnects," in *IEEE Custom Integrated Circuits Conference (CICC), 2011*, pp. 1–8.

[17] S. Chen, E. Timurdogan, M. R. Watts, and V. Stojanovic, "Integrated microring tuning in deep-trench bulk CMOS," in *IEEE Optical Interconnects Conference, 2013*, pp. 54–55.

[18] M. S. Nawrocka, T. Liu, X. Wang, and R. R. Panepucci, "Tunable silicon microring resonator with wide free spectral range," *Applied Physics Letters*, vol. 89, no. 7, pp. –, 2006.

[19] G. T. Reed, G. Mashanovich, F. Y. Gardes, and D. J. Thomson, "Silicon optical modulators," *Nat Photon*, vol. 4, no. 8, pp. 518–526, 2010. 10.1038/nphoton.2010.179.

[20] K. Kenta, T. Tetsuo, and S. Hideo, "An infrared silicon optical modulator of metaloxidesemiconductor capacitor based on accumulation-carrier absorption," *Japanese Journal of Applied Physics*, vol. 48, no. 4S, p. 04C107, 2009.

[21] P. Dong, W. Qian, H. Liang, R. Shafiiha, D. Feng, G. Li, J. E. Cunningham, A. V. Krishnamoorthy, and M. Asghari, "Thermally tunable silicon racetrack resonators with ultralow tuning power," *Optics Express*, vol. 18, no. 19, pp. 20298–20304, 2010.

[22] Q. Xu, B. Schmidt, S. Pradhan, and M. Lipson, "Micrometre-scale silicon electro-optic modulator," *Nature*, vol. 435, no. 7040, pp. 325–327, 2005.

[23] D. Rabus, *Integrated ring resonators: the compendium*. Berlin: Springer, 2007.

[24] W. Bogaerts, P. De Heyn, T. Van Vaerenbergh, K. De Vos, S. Kumar Selvaraja, T. Claes, P. Dumon, P. Bienstman, D. Van Thourhout, and R. Baets, "Silicon microring resonators," *Laser & Photonics Reviews*, vol. 6, no. 1, pp. 47–73, 2012.

[25] M. R. Reshotko, D. L. Kencke, and B. Block, "High-speed CMOS-compatible photodetectors for optical interconnects," vol. 5564 of *Society of Photo-Optical Instrumentation Engineers (SPIE) Conference Series*, pp. 146–155. 10.1117/12.557049.

[26] A. O. Splett, T. Zinke, B. Schueppert, K. Petermann, H. Kibbel, H.-J. Herzog, and H. Presting, "Integrated optoelectronic waveguide detectors in sige for optical communications," *Proc. SPIE*, vol. 2550, pp. 224–234, 1995. 10.1117/12.221403.

[27] J. S. Orcutt, A. Khilo, C. W. Holzwarth, M. A. Popovi, H. Li, J. Sun, T. Bonifield, R. Hollingsworth, F. X. Krtner, H. I. Smith, V. Stojanovi, and R. J. Ram, "Nanophotonic integration in state-of-the-art CMOS foundries," *Optics Express*, vol. 19, no. 3, pp. 2335–2346, 2011.

[28] A. V. Krishnamoorthy, Z. Xuezhe, L. Guoliang, Y. Jin, T. Pinguet, A. Mekis, H. Thacker, I. Shubin, L. Ying, K. Raj, and J. E. Cunningham, "Exploiting CMOS manufacturing to reduce tuning requirements for resonant optical devices," *IEEE Photonics Journal,*, vol. 3, no. 3, pp. 567–579, 2011.

[29] W. Bogaerts, D. Van Thourhout, and R. Baets, "Fabrication of uniform photonic devices using 193nm optical lithography in silicon-on-insulator," in *14th European Conference on Integrated Optics*, pp. 359–362.

[30] S. T. Chu, B. E. Little, P. Wugen, T. Kaneko, S. Sato, and Y. Kokubun, "An eight-channel add-drop filter using vertically coupled microring resonators over

a cross grid," *IEEE Photonics Technology Letters,*, vol. 11, no. 6, pp. 691–693, 1999.

[31] C. Holzwarth, T. Barwicz, M. Popovi, P. Rakich, E. Ippen, F. Krtner, and H. I. Smith, "Accurate resonant frequency spacing of microring filters without postfabrication trimming," *Journal of Vacuum Science & Technology B*, vol. 24, no. 6, pp. 3244–3247, 2006.

[32] Q. Xu, B. Schmidt, J. Shakya, and M. Lipson, "Cascaded silicon micro-ring modulators for WDM optical interconnection," *Optics Express*, vol. 14, no. 20, pp. 9431–9435, 2006.

[33] S. Xiao, M. H. Khan, H. Shen, and M. Qi, "Multiple-channel silicon micro-resonator based filters for WDM applications," *Optics Express*, vol. 15, no. 12, pp. 7489–7498, 2007.

[34] M. S. Dahlem, C. W. Holzwarth, A. Khilo, F. X. Krtner, H. I. Smith, and E. P. Ippen, "Reconfigurable multi-channel second-order silicon microring-resonator filterbanks for on-chip WDM systems," *Optics Express*, vol. 19, no. 1, pp. 306–316, 2011.

[35] K. Padmaraju and K. Bergman, "Resolving the thermal challenges for silicon microring resonator devices," *Lateral*, vol. 60, no. 1554.7, p. 1554.8, 2013.

[36] K. Padmaraju, J. Chan, L. Chen, M. Lipson, and K. Bergman, "Thermal stabilization of a microring modulator using feedback control," *Optics Express*, vol. 20, no. 27, pp. 27999–28008, 2012.

[37] K. Padmaraju, J. Chan, L. Chen, M. Lipson, and K. Bergman, "Dynamic stabilization of a microring modulator under thermal perturbation," in *Optical Fiber Communication Conference*, p. OW4F. 2, Optical Society of America.

[38] K. Padmaraju, D. F. Logan, J. J. Ackert, A. P. Knights, and K. Bergman, "Microring resonance stabilization using thermal dithering," in *IEEE Optical Interconnects Conference, 2013*, pp. 58–59.

[39] T. Hayashi, "An innovative bonding technique for optical chips using solder bumps that eliminate chip positioning adjustments," *IEEE Transactions on Components, Hybrids, and Manufacturing Technology*, vol. 15, no. 2, pp. 225–230, 1992.

[40] J. H. Lau, *Flip chip technologies*. New York : McGraw-Hill, 1996. Includes bibliographical references and index.

[41] K. Goossen, J. Walker, S. Hui, B. Tseng, R. Leibenguth, D. Kossives, D. Bacon, D. Dahringer, and L. Chirovsky, "GaAs MQW modulators integrated with silicon CMOS," *IEEE Photonics Technology Letters*, vol. 7, no. 4, pp. 360–362, 1995.

[42] D. L. Mathine, "The integration of III-V optoelectronics with silicon circuitry," *IEEE Journal of Selected Topics in Quantum Electronics*, vol. 3, no. 3, pp. 952–959, 1997.

[43] D. R. Rolston, D. V. Plant, T. H. Szymanski, H. S. Hinton, W. Hsiao, M. H. Ayliffe, D. Kabal, M. B. Venditti, P. Desai, and A. V. Krishnamoorthy, "A hybrid-SEED smart pixel array for a four-stage intelligent optical backplane demonstrator," *IEEE Journal of Selected Topics in Quantum Electronics*, vol. 2, no. 1, pp. 97–105, 1996.

[44] F. Blom, D. Van Dijk, H. Hoekstra, A. Driessen, and T. J. Popma, "Experimental study of integrated-optics microcavity resonators: Toward an all-optical switching device," *Applied Physics Letters*, vol. 71, no. 6, pp. 747–749, 1997.

[45] I.-L. Gheorma and R. Osgood Jr, "Fundamental limitations of optical resonator based high-speed EO modulators," *IEEE Photonics Technology Letters,*, vol. 14, no. 6, pp. 795–797, 2002.

[46] T. A. Ibrahim, W. Cao, Y. Kim, J. Li, J. Goldhar, P.-T. Ho, and C. H. Lee, "All-optical switching in a laterally coupled microring resonator by carrier injection," *IEEE Photonics Technology Letters,*, vol. 15, no. 1, pp. 36–38, 2003.

[47] V. R. Almeida, C. A. Barrios, R. R. Panepucci, and M. Lipson, "All-optical control of light on a silicon chip," *Nature*, vol. 431, no. 7012, pp. 1081–1084, 2004.

[48] M. B. J. Diemeer, "Polymeric thermo-optic space switches for optical communications," *Optical Materials*, vol. 9, no. 14, pp. 192–200, 1998.

[49] G. Li, X. Zheng, J. Yao, H. Thacker, I. Shubin, Y. Luo, K. Raj, J. E. Cunningham, and A. V. Krishnamoorthy, "25gb/s 1v-driving CMOS ring modulator with integrated thermal tuning," *Optics Express*, vol. 19, no. 21, pp. 20435–20443, 2011.

[50] M. R. Watts, "Adiabatic microring resonators," *Optics Letters*, vol. 35, no. 19, pp. 3231–3233, 2010.

[51] X. Zheng, Y. Luo, G. Li, I. Shubin, H. Thacker, J. Yao, K. Raj, J. E. Cunningham, and A. V. Krishnamoorthy, "Enhanced optical bistability from self-heating due to free carrier absorption in substrate removed silicon ring modulators," *Optics Express*, vol. 20, no. 10, pp. 11478–11486, 2012.

[52] C. Chin-Hui, L. Cheng, B. Rui, A. Shafik, M. Fiorentino, P. Zhen, P. Chiang, S. Palermo, and R. Beausoleil, "Hybrid integrated DWDM silicon photonic

transceiver with self-adaptive CMOS circuits," in *IEEE Optical Interconnects Conference, 2013*, pp. 122–123.

[53] L. Cheng, B. Rui, A. Shafik, E. Z. Tabasy, T. Geng, M. Chao, C. Chin-Hui, P. Zhen, M. Fiorentino, P. Chiang, and S. Palermo, "A ring-resonator-based silicon photonics transceiver with bias-based wavelength stabilization and adaptive-power-sensitivity receiver," in *IEEE International Solid-State Circuits Conference Digest of Technical Papers (ISSCC), 2013*, pp. 124–125.

[54] F. Y. Liu, D. Patil, J. Lexau, P. Amberg, M. Dayringer, J. Gainsley, H. F. Moghadam, Z. Xuezhe, J. E. Cunningham, A. V. Krishnamoorthy, E. Alon, and R. Ho, "10-gbps, 5.3-mw optical transmitter and receiver circuits in 40-nm CMOS," *IEEE Journal of Solid-State Circuits,*, vol. 47, no. 9, pp. 2049–2067, 2012.

[55] C. Sun, M. Georgas, J. S. Orcutt, B. R. Moss, Y. H. Chen, J. Shainline, M. Wade, K. Mehta, K. Nammari, E. Timurdogan, D. Miller, O. Tehar-Zahav, Z. Sternberg, J. C. Leu, J. Chong, R. Bafrali, G. Sandhu, M. Watts, R. Meade, M. A. Popovic, R. J. Ram, and V. Stojanovic, "A monolithically-integrated chip-to-chip optical link in bulk CMOS," in *2014 Symposium on VLSI Circuits Digest of Technical Papers,*, pp. 1–2.